Water Resources Research

RESEARCH ARTICLE

10.1029/2023WR036244

Key Points:

- Floodplain caused the secondary circulation, and its intensity and scale increased as the floodplain size increased
- Strong secondary circulation destroyed the separation zone near the bed and resulted in local rise of the water surface
- A conceptual model was proposed to summarize the hydrodynamic characteristics of confluence with tributary floodplain

Correspondence to:

S. Yuan,
yuansaiyu@hhu.edu.cn

Citation:

Yan, G., Yuan, S., Tang, H., Xu, D., Liu, M., Whittaker, C., & Gualtieri, C. (2024). Hydrodynamic response of channel flow confluence to the tributary floodplain topography. *Water Resources Research*, *60*, e2023WR036244. https://doi.org/10.1029/2023WR036244

Received 24 SEP 2023
Accepted 3 AUG 2024

Hydrodynamic Response of Channel Flow Confluence to the Tributary Floodplain Topography

Guanghui Yan[1], Saiyu Yuan[1,2], Hongwu Tang[1,2], Dong Xu[2], Mengyang Liu[2], Colin Whittaker[3], and Carlo Gualtieri[4]

[1]The National Key Laboratory of Water Disaster Prevention, Hohai University, Nanjing, China, [2]Key Laboratory of Hydrologic-Cycle and Hydrodynamic-System of Ministry of Water Resources, Hohai University, Nanjing, China, [3]Department of Civil and Environmental Engineering, The University of Auckland, Auckland, New Zealand, [4]Department of Structures for Engineering and Architecture, University of Napoli Federico II, Napoli, Italy

Abstract River confluences with a compound-channel tributary are common in large river networks, for example, the Yangtze River basin and the Amazon basin. They affect the confluence hydrodynamics, nutrient depletion and fish migration in the network, due to the seasonal exposure and submergence of the tributary floodplain. The corresponding influencing mechanisms are critical but poorly understood. This study investigated the hydrodynamic response of channel flow confluence to the tributary floodplain, that is, various widths and heights of the floodplain. Two kinds of secondary circulations were identified: One was due to the tributary streamline curvature, and the other produced by flow separation in the floodplain step. An increase in the floodplain size enhanced the strength of the secondary circulation in the compound tributary channel, but it disappeared near the junction because of the effects of the main channel. The decreased tributary cross-sectional area amplified the flow momentum, resulting in a larger separation zone near the tributary-side wall. The strength of floodplain-induced secondary circulation increased as the floodplain width increased, and it moved toward the tributary-side bank destroying the separation zone. Moreover, strong upwelling in the secondary circulation caused the rising water surface in the separation zone, which was supposed to be a region of falling water surface caused by energy loss and negative pressure. A conceptual model was proposed to summarize the hydrodynamics of confluence with different tributary floodplain topography. Our results provided a comprehensive knowledge of the confluence hydrodynamics, which have important implication for the flood management and ecological restoration of river basin.

1. Introduction

River networks, characterized by the convergence of streams at confluences and the division of flows at bifurcations, constitute complex and multi-threaded systems that hold significant economic and ecological value (Palmer & Ruhi, 2019; Tonkin et al., 2018). The evolution of river networks and their flow connectivity, which governs the distribution of water and its response to local disturbances, has critical importance for both human society (e.g., water resource management, flood defense) and ecosystems (Messager et al., 2021). Confluences, serving as primary nodes within river network systems, exert significant influences on flow hydrodynamics, sediment and contaminant transport, as well as riverine aquatic ecology, and have thus received increasing attention in recent years (Canelas et al., 2022; Duguay et al., 2022; Gualtieri et al., 2019, 2020; Sukhodolov et al., 2022; Yuan, Xu, Tang, Xiao, & Whittaker, 2022). A comprehensive understanding of the flow dynamics at confluences, is therefore of crucial importance in advancing the management and restoration of river network systems (Tang et al., 2022; Vári et al., 2022).

Confluence hydrodynamics have been extensively investigated (Best, 1987; Best & Roy, 1991; Bradbrook et al., 2001; Constantinescu et al., 2012; Canelas et al., 2020; Gaudet & Roy, 1995; Gurram et al., 1997; Gualtieri et al., 2019; Jin et al., 2023; Mosley, 1976; Rhoads & Sukhodolov, 2004; Sukhodolov & Sukhodolova, 2019; Yuan, Xu, Tang, Xiao, & Gualtieri, 2022, 2024). Mosley (1976) firstly attempted to present a general model of confluence hydraulics. Best (1987) proposed a conceptual model that identifies six distinct hydrodynamic regions in the confluence hydrodynamics zone (CHZ), namely flow stagnation, flow deflection, flow separation, flow acceleration, flow recovery, and shear layers. Different momentum ratios (M_r) and junction angles of confluent flows create various flow structures and features. A separation zone develops at the downstream junction where the flow has sufficient momentum to detach from the channel wall, and its size increases with higher momentum ratios and junction angles (Gurram et al., 1997). The shear layer occurs at the interface between the two confluent flows, characterized by a von Kármán vortex street for $M_r \approx 1$ (Constantinescu et al., 2012) or vortex pairing that suggests the dominance of KH (Kelvin-Helmholtz) vortices for $M_r \neq 1$ (Rhoads & Sukhodolov, 2004). Helical motions emerge as a prominent hydrodynamic feature at confluences, which can be attributed to the imbalance between centrifugal and pressure-gradient forces within the spatial domain. The mutual flow deflection results in single or dual secondary circulations at different junction angles (Rhoads et al., 2009).

Notably, bathymetric surveys in natural confluences have revealed bed discordance (defined as a difference in bed elevation between two incoming channels). Best and Roy (1991) firstly reported that bed discordance modified flow structure creating a distortion of the shear layer and fluid upwelling at the downstream junction corner. Gaudet and Roy (1995) showed that bed discordance can markedly increase mixing rates and the mixing distances are 5–10 times shorter than previously reported. Bed discordance significantly enhanced the intensity of secondary circulation, consequently, leading to the flow separation zone being absent near the bed (Biron et al., 1996; Bradbrook et al., 2001). The tributary flow mainly penetrates the main channel around the free surface, whereas the near-bed flow from the main channel progresses underneath the tributary inflow practically unimpeded by the confluence, resulting in a two-layer flow structure (Guillen-Ludena et al., 2017; Leite Ribeiro et al., 2012). In scenarios characterized by a higher degree of bed discordance with increased tributary flow velocity, a cross-sectional scale recirculation cell in the lee of the backward-facing step of the tributary destroyed the two-layers flow structure (Canelas et al., 2020, 2022).

However, in many river networks, especially those in lowland area, a large floodplain exists at the tributary bank near the side of the upstream junction partially occupying the tributary width, which submerged or exposed due to the large variation in the tributary water levels (Figure 1). Depending on whether the floodplain is submerged or emerged, the tributary may act as a compound channel or as a single channel, respectively. This floodplain in tributary, on the one hand, may be related to the evolution of riverbed over a long period and weak hydrodynamics near the flow stagnation zone (De Morais et al., 2016; Marinho et al., 2022). On the other hand, changes during the hydrological year in the discharge ratio might result in the main channel flowing backwards into the tributary (Ford et al., 2020; Li et al., 2022). For example, in the Poyang Lake basin, the influence of the Three Gorges Project regulation and extreme weather has led to floodplain wetlands in a dynamic cycle of inundation to exposure, affecting flood defenses and ecosystems in the Poyang Lake basin (Mu et al., 2022; Zhang et al., 2015).

If the floodplain is submerged the tributary acts as a compound channel, where the flow structure is complicated by the large mixing layers and secondary currents resulting from the flow depth and velocity differences between the main channel and the floodplain (Singh et al., 2020; Wormleaton, 1996). Moreover, the flow structure is generally affected by the shape of the floodplain, the relative depth, and the relative velocity (Hamidifar et al., 2016; Proust & Nikora, 2020). At the confluence between the Yangtze River and the Poyang Lake (Figures 1a) and Li et al. (2022) found that the dual counter rotating helical cells and mixing interface shifted farther downstream of the junction and closer to the right bank in the condition with the floodplain flow. At the confluence of the Negro and Blanco rivers in the Amazon basin (Figure 1d), the strong backwater effect results in lower flow velocities at the confluent apex and contributes to the formation of tributary floodplain, with complex hydrodynamics and mixing process at hundreds of kilometers downstream (Marinho et al., 2022). Yuan et al. (2023) studied the influence of the tributary floodplain in a 60° laboratory-scale confluence and found a strong recirculation cell and wider separation zone downstream of the confluence, which was different from the findings in bed concordant and discordant confluences. To summarize, the shape and status of the floodplain can result in the adjustment of the flow structure in the tributary and hence of the hydrodynamics at the confluence (Figure 1). However, a complete knowledge of the effects of floodplain topography on confluence hydrodynamics is largely missing.

In the present manuscript, the results from an experimental and numerical study conducted at a laboratory-scale confluence with the tributary floodplain are reported, and compared with those observed in the field at the confluence between the Yangtze River and the Poyang Lake. The present study aims to (a) explain the mechanism of formation of secondary circulations and separation zone observed in two cases (tributary compound channel vs. tributary single channel); (b) identify the effects of floodplain topography on the dynamics of the separation zone, secondary circulations, and shear layer; (c) present a conceptual model to investigate how the tributary floodplain affects confluence hydrodynamics.

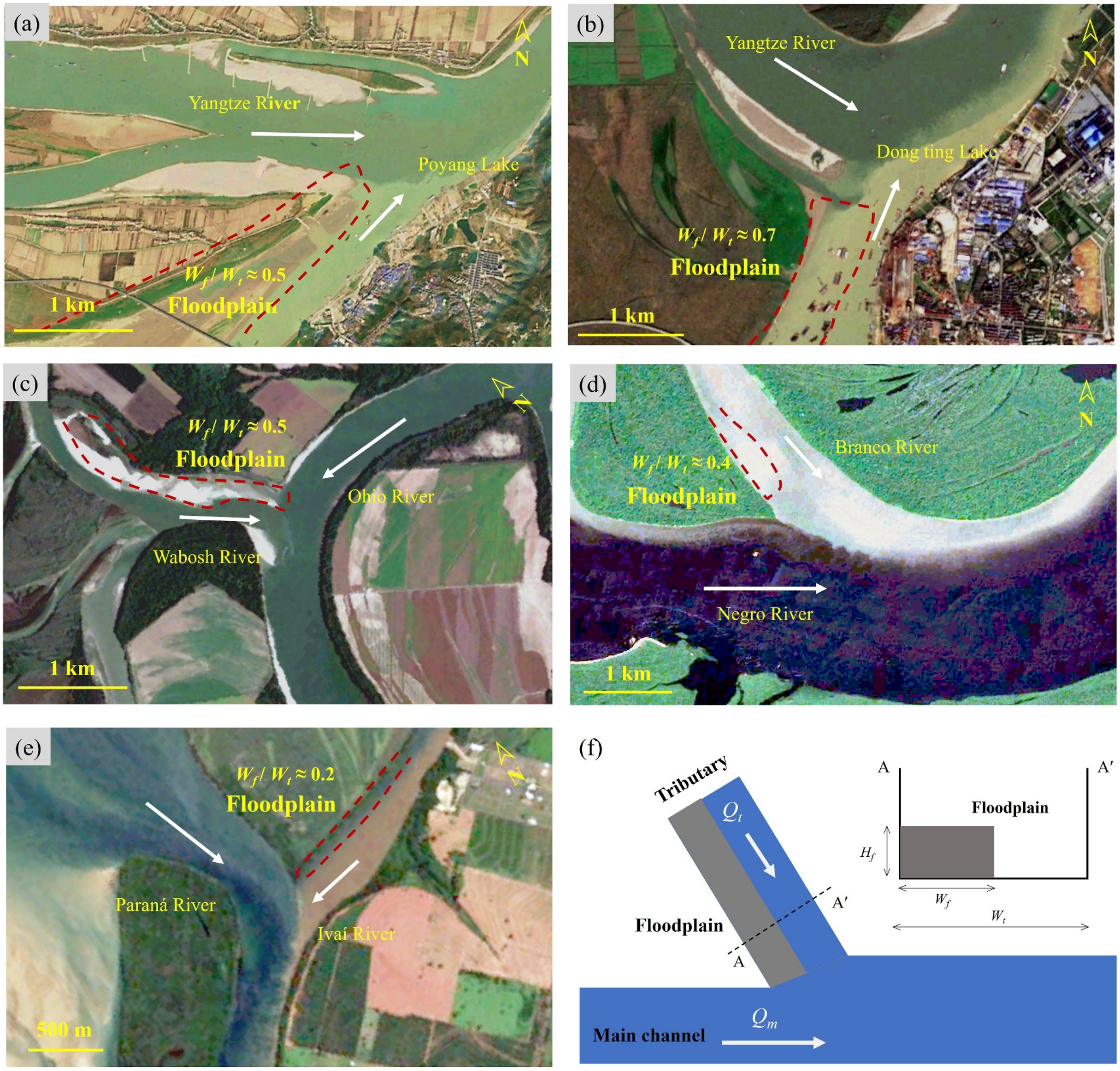

Figure 1. Some river confluences with tributary floodplain: (a) the confluence between Yangtze River and Poyang Lake (China) 29°45′N, 116°14′E; (b) the confluence between Yangtze River and Dongting Lake (China) 29°27′N, 113°9′E; (c) the confluence between Ohio River and Wabosh River (United States of America) 37°48′N, 88°1′W; (d) the confluence between Negro River and Branco River (Brazil) 1°23′S, 61°50′W; (e) the confluence between Paraná River and Ivaí River (Brazil) 23°20S, 53°43′W. (f) Sketch of confluence with a tributary floodplain. Satellite images are form Landsat.

2. Methodology

2.1. Experimental Setup and Instrumentation

Experimental data were collected in a 60-degree laboratory-scale confluence at Hohai University. The straight upstream channels were each 3 m long, 0.32 m wide, and 0.4 m deep, while the post-confluence channel was longer (7 m) and slightly wider ($W = 0.42$ m). To represent an idealized floodplain on the left side, a plexiglass cuboid, extending over the full length of the tributary channel, and having a downstream cross-section in the vertical plane connecting the upstream and downstream edges of the junction, was used. The floodplain was 0.16 m (W_f) in width and 0.1 m (H_f) in height. Three-component instantaneous velocities were acquired using an acoustic Doppler velocimeter (ADV) at a sampling frequency of 100 Hz for 120 s per point. The Arrangement of measurement points is shown in Figure 2. In each cross section, the transverse spacing of the measured profiles was 2 cm, and the vertical spacing between two adjacent measurement points was 1 cm (Figure 2b). The x, y, z

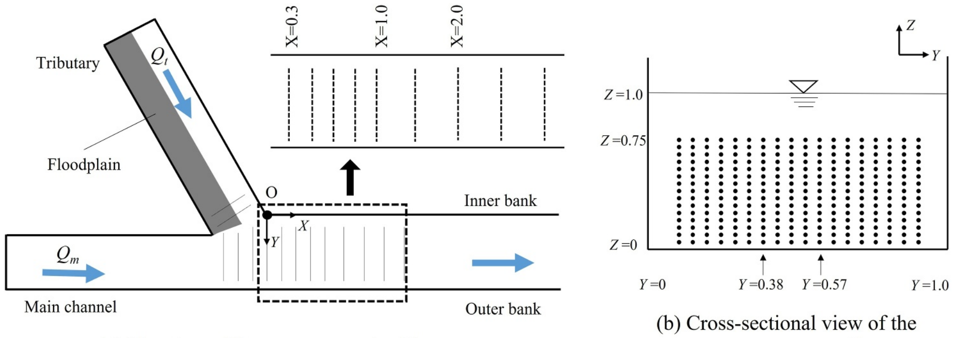

(a) Planview of the measurement grid

(b) Cross-sectional view of the measurement grid

Figure 2. Location of the points of measurement.

coordinate system has an origin at the bed in the downstream junction corner. The results are presented along dimensionless coordinates, using the width of post-confluence channel W and the flow depth H.

The discharges in the tributary and the main channel were 7 and 10 L/s, respectively, resulting in a discharge ratio ($Q_r = Q_t/Q_m$) of approximately 0.7. The downstream water level was adjusted using a tailgate, and the flow parameters are summarized in Table 1. The first case, Run F0, served as a reference case. The second case, Run F1, was undertaken to identify the impact of the absence of floodplain on the flow structure. The flume experiments in this study are mainly used to validate the accuracy of the mathematical model, and the detailed analysis of the experiments, the reader is referred to Yuan et al. (2023).

2.2. Mathematical Model

The flow has been solved using the Reynolds-averaged Navier-Stokes (RANS) equations for conservation of mass and momentum. The RANS equations for an incompressible fluid under the Boussinesq assumption are:

$$\frac{\partial u_i}{\partial x_i} = 0 \tag{1}$$

$$\frac{\partial u_i}{\partial t} + u_j \frac{\partial u_i}{\partial x_j} = -\frac{1}{\rho}\frac{\partial P}{\partial x_i} + \frac{\partial}{\partial x_j}\left[\nu\left(\frac{\partial u_i}{\partial x_j} + \frac{\partial u_j}{\partial x_i}\right)\right] + \frac{\partial}{\partial x_j}\left(\nu_t\left(\frac{\partial u_i}{\partial x_j} + \frac{\partial u_j}{\partial x_i}\right)\right) \tag{2}$$

where P is the piezometric pressure, x_i ($i = 1, 2, 3$) is the coordinates in the cartesian coordinate system, u_i, u_j (i, $j = 1, 2, 3$) is the velocity components, t is the time, ρ is the water density, ν is the kinematic viscosity of the water; ν_t is the kinematic eddy viscosity.

The VOF approach was applied, which captures the interface between the phases by determining a continuity equation for the volume fraction of the water phase (Hirt & Nichols, 1981). The formula may be written as:

$$\frac{\partial \nu_w}{\partial t} + \frac{\partial(\alpha_w u_i)}{\partial x_i} = 0 \tag{3}$$

Table 1
Characteristics of the Two Runs

Run ID	Tributary discharge Q_t (l/s)	Main channel discharge Q_m (l/s)	Flow depth H (m)	Discharge ratio Q_r (−)	Momentum flux ratio M_r (−)	The width of floodplain W_f (m)	The height of floodplain H_f (m)
F0	7	10	0.2	0.7	0.49	0.0	0.0
F1	7	10	0.2	0.7	0.65	0.16	0.10

Note. The subscripts of "m" and "t" represent the main channel and the tributary, respectively.

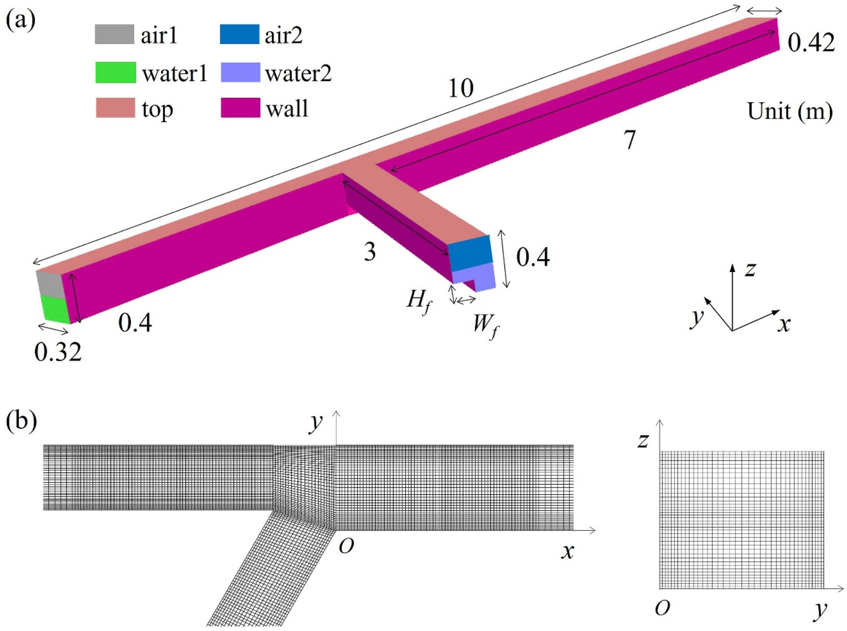

Figure 3. Domain, boundary conditions and mesh of numerical simulation.

where α_w is the volume fraction of water, which is equal to 1 when the cell is full of water, 0 when the cell is empty, and a value between 0 and 1 when the cell is in the infinitesimal region where the free surface is defined, respectively.

In this study, the three-dimensional RANS code based on the finite volume method in ANSYS Fluent is used to solve the governing equations. The Reynolds stress model (RSM) was applied as turbulence model, due to its having been extensively and successfully used for numerical modeling of free surface flows (Maranzoni & Tomirotti, 2021; Tang et al., 2018). A detailed introduction to the model is presented in Appendix A. Such model removes the isotropic eddy-viscosity hypothesis and solves the RANS equations by using transport equations for the Reynolds stresses, that is, the last term in Equation 2 is replaced by the gradient of the Reynolds stress tensor and for each Reynolds stress a transport equation is solved, together with an equation for the dissipation rate (Gibson & Launder, 1978). The computational domain meshes and boundary conditions used in the simulation were designed to match those of the laboratory experiment (Figure 3). The main channel and tributary inlet borders were divided into water-inlets and air-inlets. A pressure-outlet boundary condition was implemented at the outlet boundary. The walls were assumed to be impermeable and smooth, subject to both the standard wall function and the no-slip boundary condition (Luo et al., 2018; Momplot et al., 2017). The y^+value of the first grid cell near the wall was checked using Equations 4–6, which is consistent with previous studies (Ouro et a., 2018; Shen et al., 2022).

$$U^+ = \begin{cases} y^+ & \text{for } y^+ < 11.63 \\ \dfrac{1}{k}\ln\left(Ey^+\right) & \text{for } y^+ \geq 11.63 \end{cases} \tag{4}$$

$$U^+ = \frac{\mu {C_u}^{1/4} k^{1/2}}{\tau_w/\rho} \tag{5}$$

$$y^+ = \frac{\mu \rho {C_u}^{1/4} k^{1/2}}{u} y \tag{6}$$

where the parameters U^+ and $y^+$are both dimensionless and represent velocity and distance. K is the von Karman constant, which is equal to 0.41. E is the experimental constant and the value is on average 9.81. τ_w is the wall shear stress and k is the turbulent kinetic energy (TKE). μ is the fluid dynamic viscosity. y is the distance between the node and the wall.

The mesh was refined near the confluence zone, side walls, and free water surface to improve the accuracy and resolution of the calculation results, as shown in Figure 3b. The mesh size was chosen after conducting a mesh sensitivity analysis to ensure convergence, as shown in Appendix B. Upstream of the junction and in the post-confluence channel, the size of a single cell $\Delta x \times \Delta y \times \Delta z$ was 30*11*8 mm, while in the areas close to the walls, the $\Delta x \times \Delta y \times \Delta z$ was 15*11*8 mm. Compared to the other regions, there is a slight decrease in mesh quality near the interface between the tributary and the main channel, where the skewness of the mesh is around 0.2 and the orthogonal quality is around 0.9, still representing a good mesh quality (Fatchurrohman & Chia, 2017). The Pressure Implicit Splitting of Operator algorithm was employed for the pressure-velocity coupling (Issa, 1986). The momentum reconstruction at the faces of the computational cells was performed using a second-order upwind method, while the pressure spatial interpolation was performed using a body-force-weighted scheme. Maranzoni and Tomirotti (2021). Transient simulations were carried out utilizing a second-order implicit marching approach, which allowed for greater time steps without generating numerical instability and diffusivity. To monitor convergence, the convergence residual was set to 0.001, following Momplot et al. (2017). A variable global time step was used to advance in time to combine numerical stability and computing efficiency.

2.3. Validation of the Numerical Simulations

Run F1 was chosen for reference. For this case, the numerical model was validated by comparing the numerical results with the experimental data at the confluence zone (X = 0.3, 1.0 and 2.0). Figure 4 compares the mean velocity components (u, v, and w, respectively) for two locations (Y = 0.38 and Y = 0.57) near the secondary motions. For the lateral velocity v and vertical velocity w, the errors of the simulation were relatively larger, but the trend of vertical distribution was consistent with the experimental data. The area with significant deviation was located at the depth of Z = 0.3–0.5, as shown in Figures 4b and 4c (X = 1.0, Y = 0.38 and X = 2.0, Y = 0.38). This is because at this location, the lateral velocity changes from positive to negative, and the vertical velocity peaked.

To provide a more precise evaluation of the simulation results, a quantitative assessment was conducted. The key residual criteria were: Bias, Mean Square Error (MSE), Root Mean Square Error, Mean Absolute Error and Absolute Maximum Error, as introduced by Blocken and Gualtieri (2012). These criteria were used to validate simulated cross-sectional velocity, and the resulting error statistics are listed in Table 2. Small values (in absolute terms for the key residual criteria) indicate better agreement with experimental data. The error statistics of the numerical results were reasonable for the 3D velocity.

Figure 5 shows the cross-sectional distribution of the velocity components, the water surface profile and the TKE for both the numerical results and experimental data. The separation zone, characterized by a negative or low streamwise velocity, was observed on the left side of the channel, with a width of 0.18 W at X = 0.3 and gradually narrowed downstream (Figure 5a). The numerical results showed that the separation zone was relatively small near the junction corner (X = 0.3), and the width and length of the separation zone were slightly larger than those observed in the laboratory experiments (X = 1.0 and 2.0). Just near the junction, it was difficult to accurately capture the characteristics of the separation zone, where, but at downstream the numerical model was able to approximately simulate the separation zone. Moreover, the core of the secondary flow was found to be located at Y = 0.4, Z = 0.4 in the experimental data and Y = 0.45, Z = 0.4 in the numerical results. This also explained for large lateral and vertical velocity deviations presented in Figure 4. Additionally, the velocity of the secondary flow was more uniform without a significant peak. Despite some size deviations of secondary flow, the overall error was small and acceptable. The analysis demonstrated that the numerical model was able to reveal the characteristics of separation zone and secondary flow at CHZ.

Figure 5c shows that the numerical water surface profile matched with the experimental data. The main features of the water surface of the confluent streams were captured, including an increase of water depth upstream and a depression at the post-confluence water surface in the vicinity of junction downstream. The experimental results and numerical simulations have a large difference in the TKE distribution (Figures 5d and 5e). The numerical results can reflect the high turbulence levels at the separation zone, but when capturing the turbulence energy of the secondary flow due to the high velocity gradients, only the location was identified, while the specific TKE value cannot be accurately simulated.

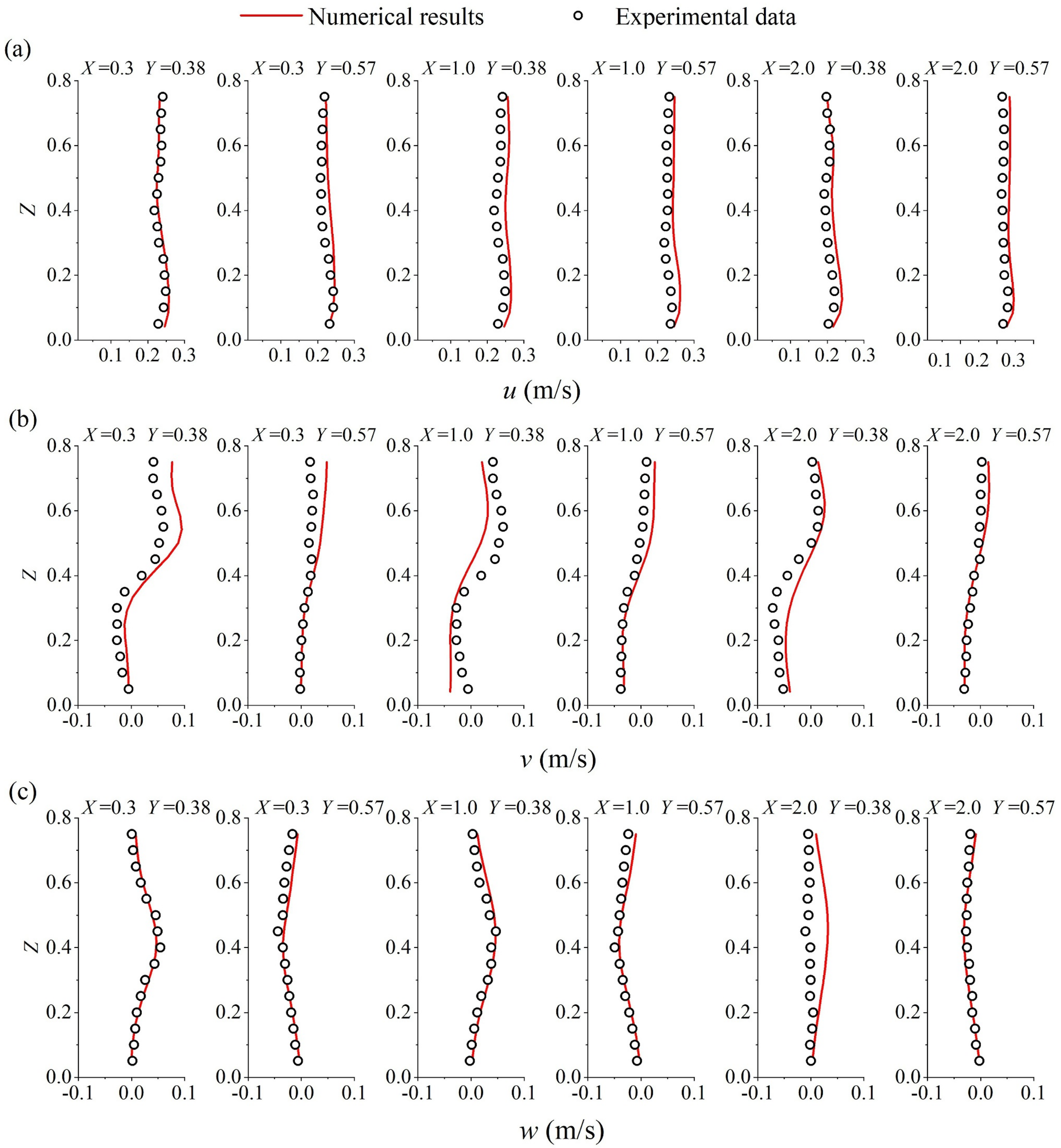

Figure 4. Comparison of numerical (line) and experimental (marker) results of the (a) streamwise velocity, (b) lateral velocity and (c) vertical velocity in different locations.

3. Results

3.1. Flow Features of the Flume Confluence

Figure 6 shows the mean flow field in Run F0 and F1 (the locations are shown in Figure 2). The typical hydrodynamic characteristics observed at confluence include a stagnation zone with lower velocity near the junction and an acceleration zone where the two streams merge (Figure 6a). The separation zone was located at the wall of

Table 2
Key Residual Criteria and Results of the Velocity

Method	Formula	Range	Ideal value	Velocity u	Velocity v	Velocity w
BIAS (m/s)	$\frac{1}{n}\sum_{i=1}^{n}\left(y_i-\hat{y}_i\right)$	$(-\infty,+\infty)$	0	−0.0111	−0.0118	−0.0034
MSE (m^2/s^2)	$\frac{1}{n}\sum_{i=1}^{n}\left(y_i-\hat{y}_i\right)^2$	$(0,+\infty)$	0	0.0005	0.0003	0.0001
RMSE (m^2/s^2)	$\sqrt{\frac{1}{n}\sum_{i=1}^{n}\left(y_i-\hat{y}_i\right)^2}$	$(0,+\infty)$	0	0.0228	0.0161	0.0099
MAE (m/s)	$\frac{1}{n}\sum_{i=1}^{n}\left\|\left(y_i-\hat{y}_i\right)\right\|$	$(0,+\infty)$	0	0.0174	0.0128	0.0063
AME (m/s)	$Max\left\|\left(y_i-\hat{y}_i\right)\right\|$	$(0,+\infty)$	0	0.0809	0.0600	0.0626

Note. y_i is the experimental value, $\hat{y}_i$ is the numerical value, MSE is Mean Square Error, RMSE is Root Mean Square Error, MAE is Mean Absolute Error, AME is Absolute Maximum Error. The above results were calculated from all the measurement points of three cross sections ($X = 0.3$, 1.0 and 2.0), each section has 270 measurement points, as shown in Figure 2b. The value of n is 810.

the post-confluence channel where negative velocity is visible, exhibiting a distinctive three-dimensional feature ($Z = 0.75$ and $Z = 0.2$). The size of the separation zone was modified by the tributary floodplain, with a noticeable 20% increase in width and a minor change in length (Figure 6b). Moreover, only one secondary flow with a rotational velocity of around 8% U_m and an area of about 0.3 W was observed because of the limited width-to-depth ratio and asymmetric platform. Due to the downstream weakening of centrifugal force, the secondary flow was no longer significant at $X = 2.5$ for F0 (Figure 6c). However, in F1, the magnitude and intensity of the secondary flow increased (having 20%–30% U_m), occupying approximately 0.5 W and extending at a far downstream distance (Figure 6d).

3.2. Flow Structure Analysis: Run F0 and F1

3.2.1. Analysis of the Separation Zone by RANS Equation

The analysis of the flow mechanism in the separation zone is important due to the enhanced momentum transfer induced by lateral currents. To this end, the non-dimensional RANS equations have been used by Schindfessel et al. (2017) to gain insights into the flow process in the separation zone. The RANS equations express the conservation of longitudinal momentum and can be written in a non-dimensional form as follows:

$$\overbrace{\frac{W}{U_m^2}\left(u_i\frac{\partial u}{\partial x_i}\right)}^{A} = -\overbrace{\frac{W}{U_m^2}\frac{1}{\rho}\frac{\partial p}{\partial x}}^{P} + u\overbrace{\frac{W}{U_m^2}\left(u_i\frac{\partial^2 u}{\partial x_i^2}\right)}^{\nu} - \overbrace{\frac{W}{U_m^2}\left(\frac{\overline{\partial u' u_i'}}{\partial x_i}\right)}^{T} \tag{7}$$

where (A) represents the advection of longitudinal momentum, (P) represents the pressure gradient, (ν) represents the viscous stresses, and (T) represents the exchange of momentum due to turbulent fluctuations.

The study focuses on a specific depth ($Z = 0.9$) that is representative of the flow processes near the surface, where the separation zone had larger sizes and was observed in both runs. The analysis begins with a discussion of Run F0 as a reference, followed by a discussion of Run F1 to address the effects of the floodplain. Figure 7 presents the different terms of Equation 7 at $X = 0.5$, 1.0, and 2.0 in both runs, where the separation zone formed, developed, and gradually disappeared (Figures 7a and 7b). Notably, the viscous term (ν) is of negligible importance far from the boundary layer.

In Run F0, the four terms trend to zero when $Y < 0.12$ (Figure 7c), after which the advection term (A) and turbulent term (T) grew quickly in the separation boundary. The advection term (A) was primarily driven by the turbulent term (T), resulting from a large flow velocity gradient and turbulence; When $Y > 0.28$, (T) was almost zero and the pressure gradient (P) was large, indicating that (A) was driven by (P), corresponding to a declining pressure and water level. This local decrease in water level has been observed in past laboratory-scale experiments (Canelas et al., 2020). At $X = 1.0$, the negative (P) on the inner bank of the channel is higher, indicating the major driver of the separation zone is the negative pressure. However, turbulent exchanges are of equal importance. The peaks of (A) and (T) both increased compared to the upstream cross section, and the corresponding positions also moved to the right ($Y = 0.24$), where the size of the separation zone was larger. At $X = 2.0$, a positive (A) near the

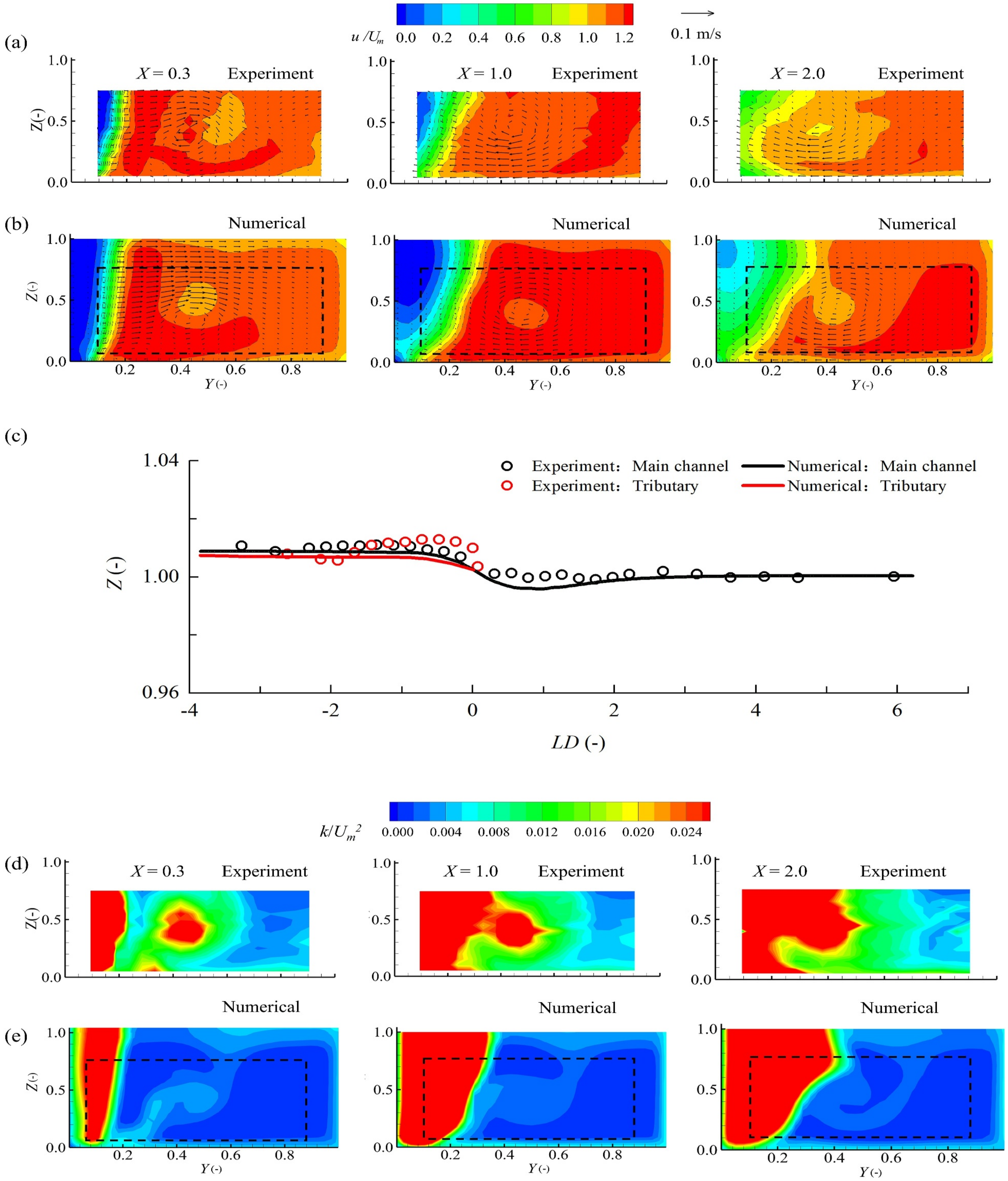

Figure 5. Comparison between the experimental data and numerical results for three cross sections at Case F1 ($X = 0.3$, 1.0 and 2.0). (a, b) are the cross-sectional distribution of the velocity components; (c) is the water surface profile at the center of channel where LD is the non-dimensional longitudinal coordinate with the zero value at the corner; (d, e) are the cross-sectional distribution of turbulent kinetic energy. The black dashed line represents the measurement area in the experiments.

left bank indicated that the flow bypasses the separation zone and flows downstream, and the lower values of the (P) also demonstrated that the separation zone gradually disappeared, which is consistent with the velocity field in Figure 7a.

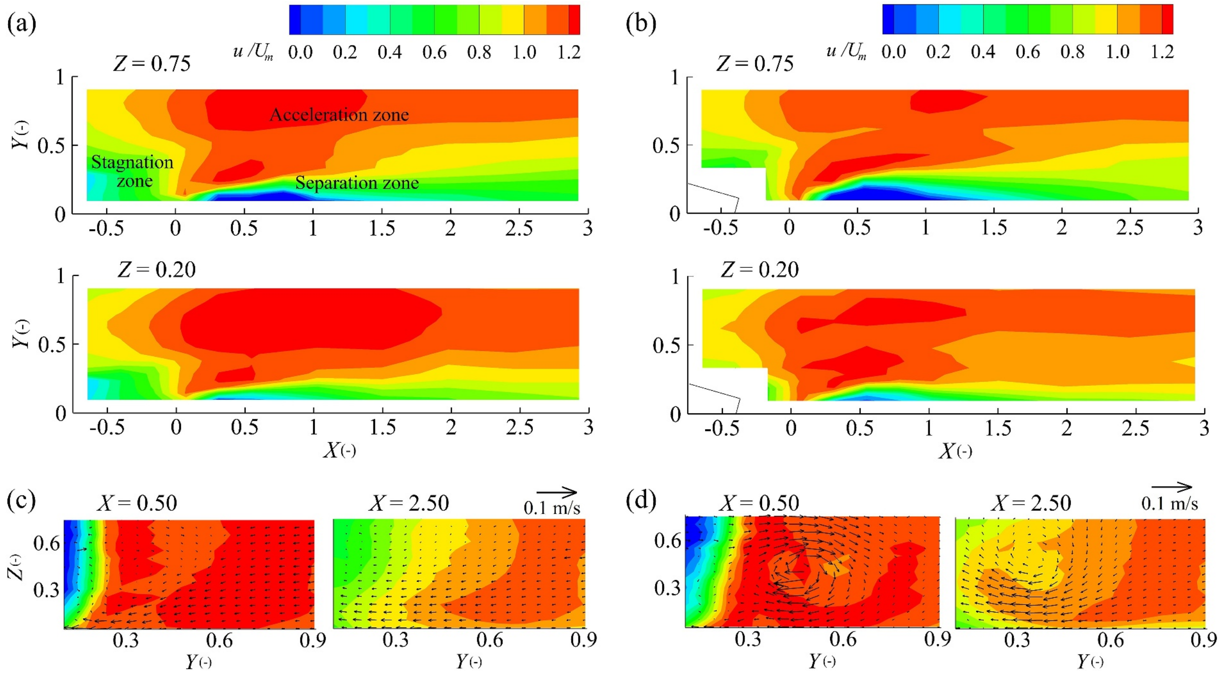

Figure 6. Mean velocity field: (a, c) Run F0; (b, d) Run F1. Vector arrows show the direction and the magnitude of (v, w) on the y-z plane.

The analysis of the dimensionless longitudinal RANS terms in the separation zone of Run F1 reveals interesting differences from Run F0. While the overall trend was similar, with the advection term (A) and turbulent term (T) growing quickly in the separation boundary, the peaks and corresponding positions of each term shifted. Specifically, at $X = 0.5$, the (A) and (T) terms increased at a longer distance from the side wall ($Y = 0.18$) compared to Run F0. Additionally, the pressure gradient (P) values are higher in the separation boundary and right bank. This pattern was even more pronounced at $X = 1.0$ and $X = 2.0$, indicating that the formation of a wider separation zone was related to higher negative pressure.

3.2.2. The Formation of Secondary Flow

The formation of secondary flow and its drivers have been extensively researched (Constantinescu et al., 2012; Sukhodolov & Sukhodolova, 2019). The secondary flows observed by Yuan et al. (2023) were possibly related to the fluid upwelling resulting from the interaction between the floodplain step and the main flow, the streamline curvature, and the effects of the helical cell in the tributary.

The tributary is a compound channel with a floodplain (Proust & Nikora, 2020), in which the helical cell must also be considered to understand the formation of secondary flow at confluence. Figure 8 presents the distribution of velocity vectors (v', w') superimposed on the contours of the streamwise velocities u' in the tributary. The x', y', z' coordinate system originates from the bed in the downstream junction corner (Figure 8a). The results are presented along dimensionless coordinates, using the width of the post-confluence channel W and the flow depth H. The results show that the typical flow structure of a compound channel was observed at $X' = 1.3$ (Figure 8b), characterized by the secondary cell and the difference in flow velocity between the tributary main channel and floodplain. However, at $X' = 0.8$, the secondary cell was destroyed, and the magnitudes of cross-sectional vectors increased. Figure 8d further reveals a stagnation zone with a low velocity above the floodplain at $Y' > 0.6$, and all the cross-sectional vectors were pointing downstream, which is likely due to the effects of higher-speed main channel flow. Therefore, the secondary cell in the tributary was only observed upstream of the confluence zone, and its effects on the secondary flow at the confluence could be neglected.

Figure 9 presents the cross-sectional distribution of the velocities at the confluence zone for Run F0 and F1. To better understand the formation of secondary flow, four cross sections ($X = -0.7$, -0.4, 0.0 and 0.5) were selected close to the floodplain step and downstream (Figure 9a). In Run F0, the whole section flow velocity vectors pointed to the outer bank at $X = -0.7$, -0.4 and 0.0, which is mainly attributed to the impact of the lateral tributary flow

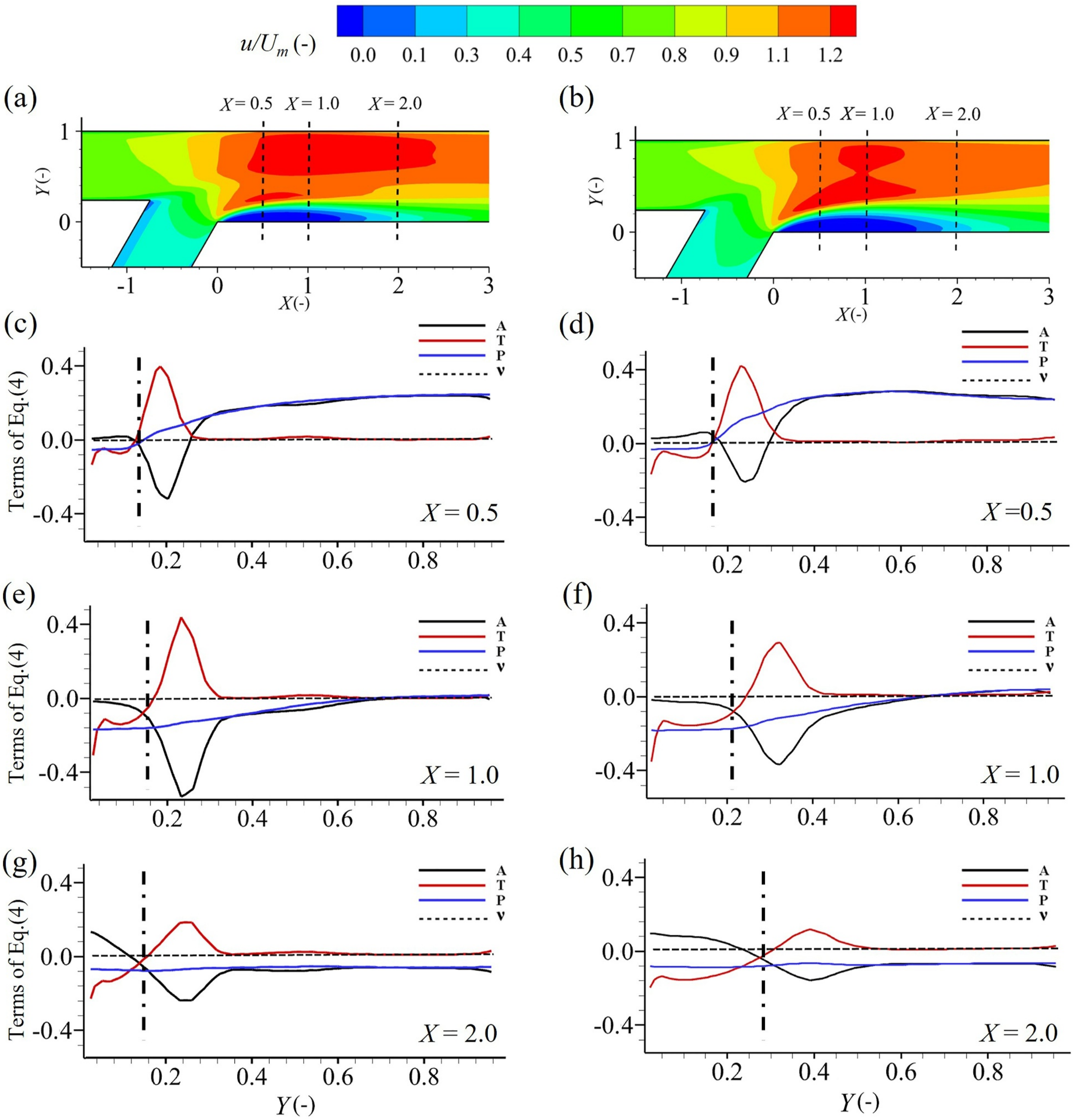

Figure 7. Terms of the dimensionless longitudinal Reynolds-averaged Navier-Stokes equation evaluated at $Z = 0.9$: (a, b) the mean velocity field at $Z = 0.9$ and map with the sections; (c, d) $X = 0.5$; (e, f) $X = 1.0$; (g, h) $X = 2.0$. Left column represents the Run F0 and right column represents the Run F1. The dash-dotted line represents the boundary of the separation zone.

(Figure 9d). The secondary cell only formed at $X = 0.5$, primarily due to the streamline curvature. In contrast, in Run F1, the downwelling flows developed in the lee of the floodplain step at $X = -0.7$, resulting from the flow separation at the brink of the floodplain step. A complete secondary cell was observed at the end of the floodplain step at $X = -0.4$ (Figure 9c). The helical cell observed in Run F1 had a larger rotational velocity and scale than this in Run F0, which is more evident in the streamline in the cross-section (Figure 9b) and the data presented in Table 3.

The weaker helical cell, identified as Cell 1 ($Y = 0.1$–0.3 and $Z = 0.0$–0.15), has a rotational velocity of 0.012–0.023 m/s and 0.2 W, which was similar in scale and location to that observed in Run F0. The stronger helical cell, identified as Cell 2 ($Y = 0.1$–0.6 and $Z = 0.3$–0.6), was located at the channel center, and its rotational velocity and

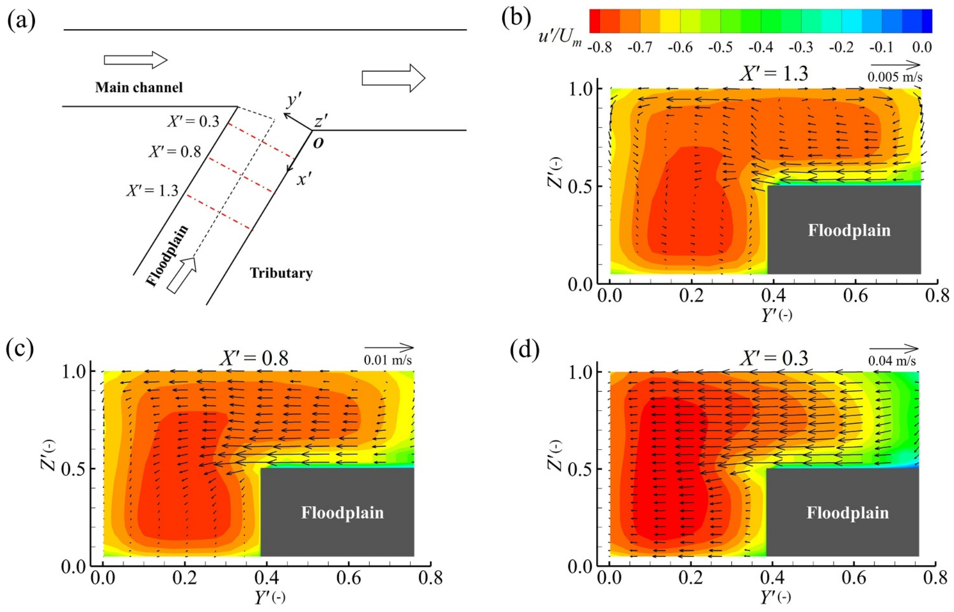

Figure 8. Cross-sectional distribution of the velocity in the tributary for Run F1: (a) Map; (b) $X' = 1.3$; (c) $X' = 0.8$; (d) $X' = 0.3$.

scale were greater than this in Run F0 (Table 3) This cell mainly resulted from the cell in the lee of the floodplain step and streamline curvature, with the effects of the floodplain playing a more significant role.

3.3. The Effects of the Tributary Floodplain on 3D Flow Structure

To examine the impact of tributary floodplain topography on the confluence hydrodynamics, a series of additional simulations were conducted with different floodplain width and height ratios (δ_w and δ_h) while keeping constant

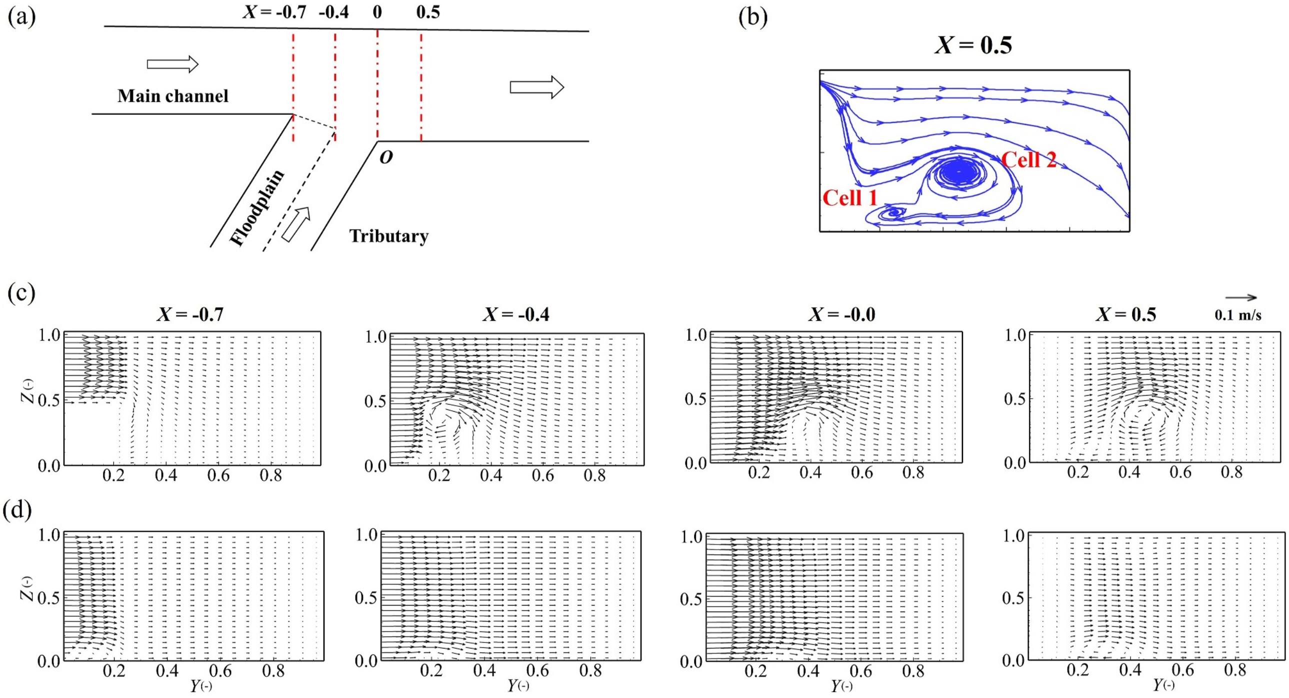

Figure 9. Cross-sectional distribution of the velocity in the main channel: (a) indication of sections; (b) flow paths at $X = 0.5$ in Run F1; (c) different cross sections in Run F1; (d) different cross sections in Run F0.

Table 3
Location, Rotational Velocity, and the Sizes of the Helical Cells at $X = 0.5$

Run	Secondary cell	Location in Y direction (−)	Location in Z direction (−)	Rotational velocity (−)	Width (−)	Height (−)
F0	Cell 1	0.1–0.3	0.0–0.15	0.06–0.12	0.14–0.19	0.05–0.15
F1	Cell 1	0.1–0.3	0.0–0.1	0.06–0.12	0.12–0.17	0.05–0.15
	Cell 2	0.1–0.6	0.3–0.6	0.16–0.27	0.29–0.38	0.50–0.60

Note. The rotational velocity is dimensional by the average velocity U_m, the width and height are dimensional by the channel width W and water depth H, respectively.

the discharge ratio Q_r (Table 4). Specifically, $\delta_w = W_f/W_t$ and $\delta_h = H_f/H$, where W_f and H_f are the floodplain width and height, W_t is the width of the tributary channel and H is the water depth. The discharge in the channels was set to 10 L/s for the main channel and 7 L/s for the tributary channel, and the water depth was set to 0.2 m.

3.3.1. Free Surface

The water surface elevation, z, normalized by the average flow depth of the post-confluence channel reach $Z_w = z/H$ ($H = 0.20$ m), is shown in Figure 10. In the main channel, the water surface gradually decreased toward the outlet of the post-confluence channel. A local rise in water level at the inner bank upstream of the junction (Figure 10a, $X = -0.8$) was observed due to the mutual deflection of both tributaries. This is commonly observed in the stagnation zone (Best, 1987; Canelas et al., 2020). Immediately downstream of the junction ($0 < X < 1.2$ and $0 < Y < 0.20$), the water surface was characterized by a local drop related to the decrease of pressure in this zone. Such a decrease in flow pressure was due to the flow separation due to abrupt shifts in the direction of the tributary flow and the associated flow detachment from the inner bank of the post-confluence channel.

The characteristics of the stagnation zone and separation zone can be observed in all simulation runs (Figure 10). As δ_w increased to 1 (bed discordance), the water surface (Figures 10d and 10h, X= 0.6–0.8) was observed to increase in the inner bank of the post-confluence channel. Such an increase was also found as the floodplain height ratio δ_h increased (Figure 10g, $X = 1.2$–1.6). This locally increase in the water surface can be attributed to flow upwelling downstream of the junction corner (see Section 3.3.4), as previously reported by Canelas et al. (2020) in confluences with bed discordance.

3.3.2. Mean Velocity Field

Figure 11 presents the cross-sectional distribution of the velocities in the tributary at different locations. Away from the confluence zone ($X' = 1.5$), the secondary flows occurring at floodplain junction region are a typical feature of compound channel (Singh et al., 2020). As the width and height of the floodplain increased, the

Table 4
Numerical Runs

Run	Relative floodplain width δ_w (−)	Relative floodplain height δ_h (−)	Velocity in tributary V_t (m/s)	Velocity ratio (V_t/V_m)	Momentum ratio M_r(−)	Reynolds number in tributary Re(−)	Froude number in tributary Fr(−)
C1	0.25	0.25	0.117	0.75	0.524	9,750	0.086
C2	0.50	0.25	0.125	0.80	0.560	9,722	0.095
C3	0.75	0.25	0.135	0.86	0.605	9,750	0.107
C4	1.00	0.25	0.146	0.93	0.654	11,303	0.120
C5	0.25	0.50	0.125	0.80	0.560	9,722	0.095
C6 (F1)	0.50	0.50	0.146	0.93	0.654	9,733	0.120
C7	0.75	0.50	0.175	1.10	0.784	9,722	0.158
C8	1.00	0.50	0.219	1.40	0.981	13,477	0.221
C9 (F0)	0	0	0.109	0.70	0.488	9,689	0.078

Note. M_r is the ratio of flow momentum, $M_r = M_t/M_m$, the momentum flux $M = \rho u Q$; R_e is the Reynolds number, $R_e = uR/v$, where u is the flow velocity, R is hydraulic radius and v is the water kinematic viscosity; F_r is the Froude number, $F_r = u/(gh)^{1/2}$, where h is flow depth. The subscripts of "m" and "t" represent the main channel and the tributary, respectively.

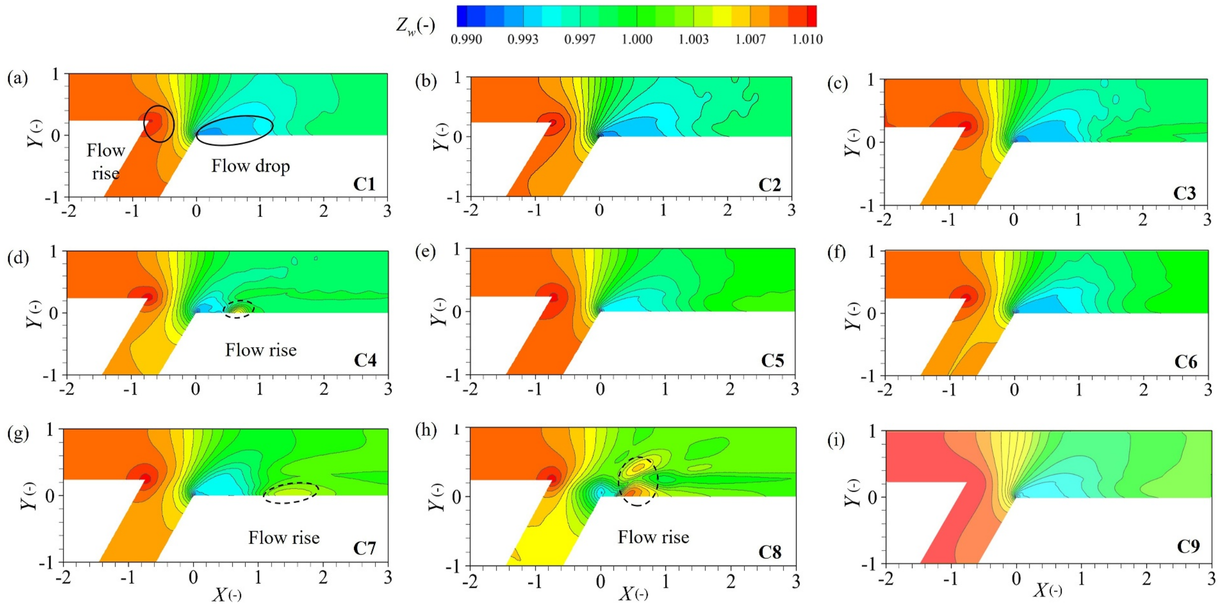

Figure 10. Normalized water surface elevation Z_w for different runs.

intensity of the secondary flows also increased significantly (Figures 11a–11e and 11g). However, due to the deflection of tributary flow and the effects of stagnation zone near the confluence, higher streamwise velocity flow was observed at the tributary right bank compare the previous section (Figure 11b, $X' = 0.5$). Moreover, the cross-sectional vectors all pointed downstream, and its values exceeded those in the $X' = 1.5$ by a factor 2–3 (Figures 11b–11f and 11h). This indicated that the increasing of the floodplain size can increase the intensity of the secondary flows in the tributary channel, but the secondary flows almost disappeared near the 0.5 W upstream of the junction point. Therefore, the effects of the secondary flows in the tributary compound channel on the confluence zone can be ignored.

Figure 12 presents the dimensionless velocity distribution at the near-water surface ($Z = 0.9$), under the floodplain ($Z = 0.2$ and $Z = 0.4$) and cross section ($X = 1.0$), respectively. In Figure 12a, the flow in the main channel significantly decelerated toward the inner bank and reached near-zero velocities in the upstream junction corner, resulting in a possible flow stagnation zone ($X = -0.8$). The main channel and the tributary both had an increase in their streamwise velocity in the confluence zone, resulting in two higher-speed zones ($Y > 0.5$ and $0.3 < Y < 0.4$) along the post-confluence channel due to the increase in flow discharge and the reduction of the effective flow cross-sectional area. Furthermore, a zone characterized by negative streamwise velocity was observed in the downstream junction corner of the confluence ($0.1 < X < 2.0$ and $Y < 0.20$). The zone complements the drop in the water surface downstream of the junction corner (Figure 10). The separation zone near the bed ($Z = 0.2$) was found to be smaller compared to that at the water surface ($Z = 0.9$), which is consistent with the 3D features reported by Schindfessel et al. (2017).

Additionally, the separation zone with a negative velocity on the inner bank and high-speed zones in the channel center are typical characteristics of CHZ (Figure 12b). However, the separation zone disappeared and was replaced by the low-velocity zone (velocity reaches 0.3–0.5U_m) as the width ratio increased. This finding has been previously reported by Guillen-Ludena et al. (2015). High streamwise velocities with the upwelling fluid were found in the main channel invading the tributary flow, destroying the separation zone ($0 < X < 0.2$ and $0 < Y < 0.5$) near the bed and squeezing this low-velocity flow into the main channel (Figure 12f). These features were even more obvious (Figure 12h) for $\delta_w = 1$, where the stronger upwelling fluid expanded the water surface and occupied approximately 20% of the width of the post-confluence channel, reaching the inner bank.

3.3.3. Stagnation Zone

The stagnation zone at the confluence originates from the corner where the flow deviates from the upstream junction and it is an area of elevated water levels and reduced flow velocities (Figures 10 and 12). The location

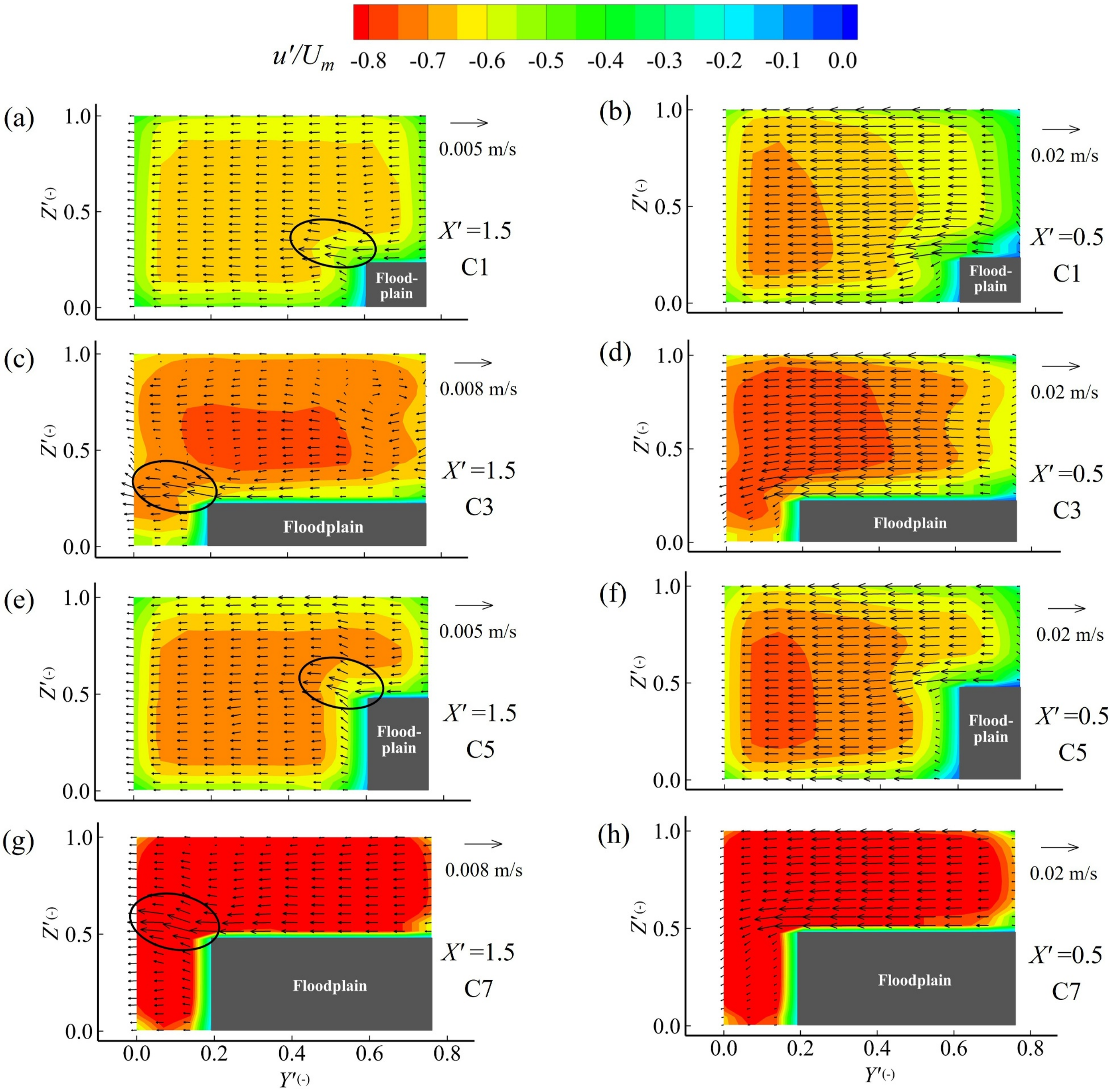

Figure 11. Distribution of the velocity vectors (v', w') superimposed on the contours of the streamwise velocities u' in the tributary: (a, b) Run C1; (c, d) Run C3; (e, f) Run C5; (g, h) Run C7. The left column is the far away from the confluence at $X' = 1.5$, the right column is near the confluence at $X' = 0.5$.

and size of the stagnation zone were identified in this study by defining a velocity-equivalent surface with velocity less than 30% U_m (Figure 13a). The stagnation zone had large planar sizes near the water surface and bed bottom ($Z > 0.8$ and $Z < 0.2$), showing a vertical distribution in the middle water depth. The stagnation zone was mainly located on the side of the tributaries, as the velocity ratio was mostly <1. A significant stagnation zone was also found above the floodplain, which gradually separated at the bed, above the floodplain, and at the water surface as the width of the floodplain increased (Figure 13b). Moreover, as the height and width of the floodplain increased, the size of the stagnation zone gradually diminished and moved to the wall of the main channel. This is due to the floodplain narrowing of the tributary overwater cross-section zone, which leading to the increase of the cross-sectional mean velocity and eventually to the equalization to the main channel velocity.

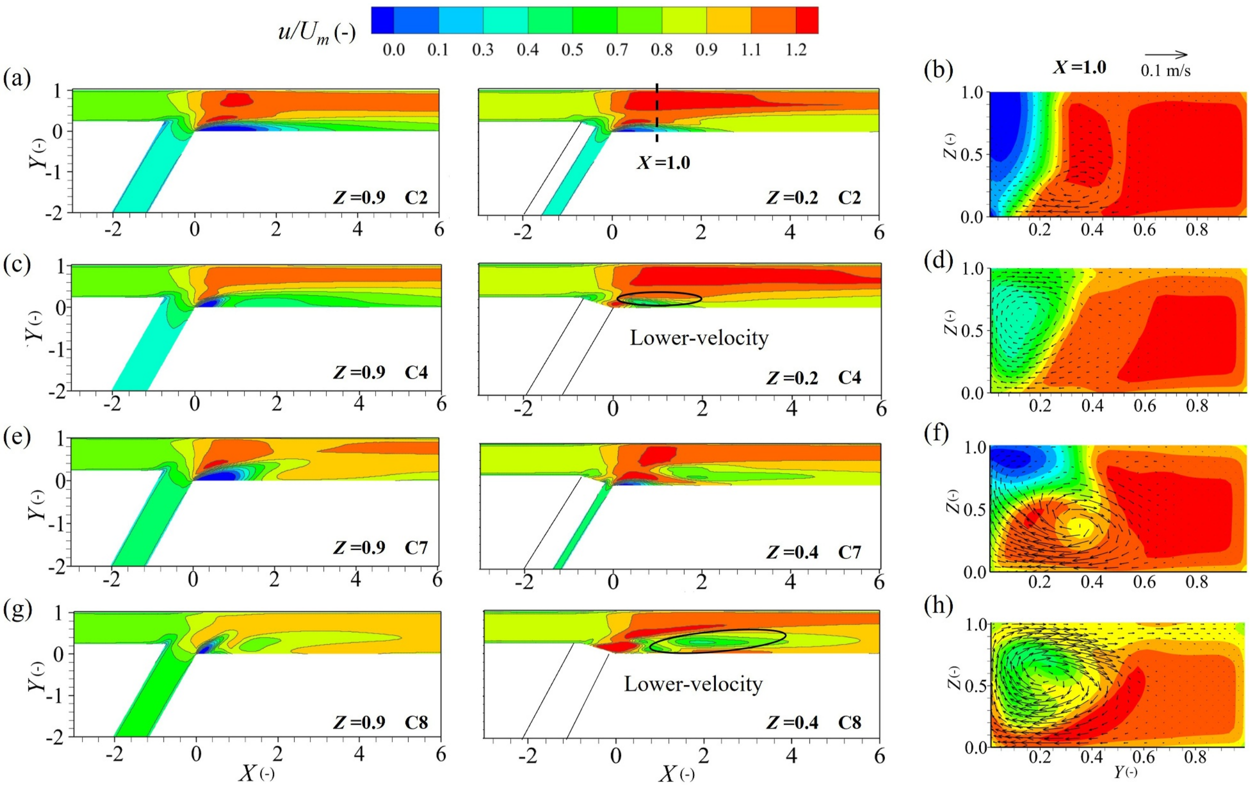

Figure 12. Mean velocity field: (a, b) Run C2; (c, d) Run C4; (e, f) Run C7; (g, h) Run C8. The left column refers to near the water surface ($Z = 0.9$) or below the floodplain ($Z = 0.2$ and 0.4), the right column is the cross-sectional velocity at $X = 1.0$. Vector arrows show the direction and the magnitude of (v, w) on the y-z plane.

3.3.4. Separation Zone

Different methods for identifying the separation zone have been proposed in the literature. The zero-discharge method, streamline method, isovel method and 3D streamline method were adopted in the previous studies (Jin et al., 2023; Schindfessel et al., 2017; Yang et al., 2009). Jin et al. (2023) systematically compared several methods and provided a detailed description of the separation zone, the recirculation zone and the reverse flow zone. In this study, the widely used contour isovel method, where the longitudinal velocity is zero, was used to distinguish the separation zone from the narrower reverse flow zone. Based on this method, two planes, close to the water surface (where the separation zone length L_s reaches a maximum, $Z = 0.9$) and the middle of the separation zone (where the separation zone width W_s peaked maximum), were considered (Figures 14b and 14c). Additionally, the shape index of the separation zone, λ_s (the maximum width W_s divided by the maximum length L_s), was considered. Moreover, because the separation zone is known to have a three-dimensional structure, different horizontal planes ($Z = 0.2$, 0.5 and 0.9) were considered, identifying the scale of the separation zone over the depth, as suggested by Best and Reid (1984) and Schindfessel et al. (2017). The sizes of the separation zone are listed in Table 5.

Based on the analysis of Figure 14b, it was found that the separation zone width in absence of a floodplain (C9) was 0.1 and 0.05 W at the water surface and the bed, respectively. However, the effects of the tributary floodplain altered this shape (C1–C8), causing an increase in the separation zone width at the surface while the separation zone at the bottom was destroyed. As δ_w and δ_h increased, the separation zone near the bed disappeared and reached a width of 0.2 W near the surface (Table 5). Additionally, the separation zone was found only for $Z > 0.7$ if δ_w was 1 (C4 and C8, Figure 14b).

The separation zone had a length of 1.2 W and a width of 0.1 W, exhibiting a flat ellipse shape at $Z = 0.9$ for the case without floodplain (C9, Figure 14c), in agreement with Best and Reid (1984). The length of the separation zone increased from 1.351 to 1.514 W as δ_w increased from 0 to 0.5, but subsequently decreased if δ_w exceeded 0.5. However, the width of the separation zone increased as both δ_w and δ_h increased (Table 5). This can be

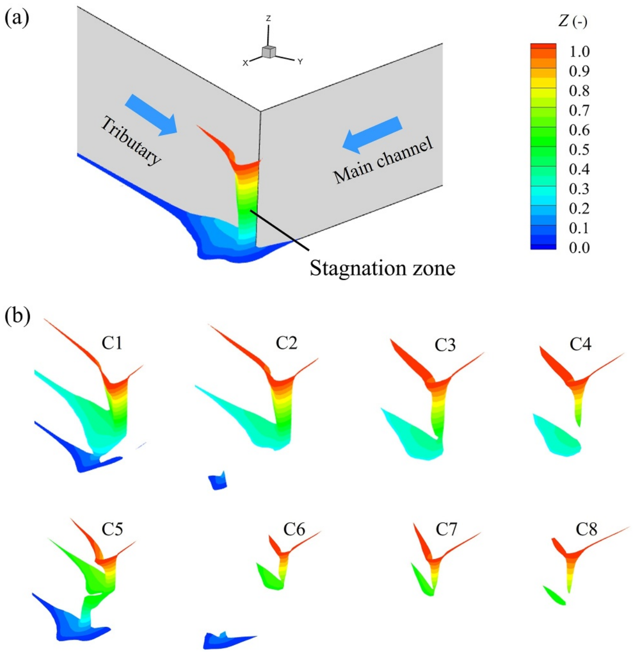

Figure 13. The location of the stagnation zone: (a) the three-dimensional structure of the stagnation zone in C9 (without tributary floodplain); (b) changes in stagnation zone for the different floodplain geometry cases (C1–C8). The boundary of the stagnation zone is defined as the equivalent surface where the u and v combined velocity reaches 30% U_m.

explained by that the floodplain restricted the cross-sectional area of the tributary flow, resulting in higher transversal velocity and more prominent flow deflection at CHZ. The length of the separation zone was destroyed by the stronger upwelling fluid at higher δ_w (Figure 14c). As the δ_h increased to 0.5, the separation zone evolved as for lower height ratio ($\delta_h = 0.25$), but more pronounced, probably for the larger velocity of the tributary flow resulting in stronger fluid upwelling downstream (Table 5).

The horizontal shape of the separation zone was found to be strongly influenced by δ_w and δ_h. Specifically, for $\delta_w = 1$, a significant change in the horizontal shape of the separation zone was observed in Figure 13c (C4 and C8). The length of the separation zone decreased by only 0.5 W, while the width expanded to 0.2 W, resulting in a convex ellipse shape. This is consistent with the results in Figure 14d, where the shape index value λ_s increased as the width and length of the floodplain increased. λ_s was found to be on average 0.1–0.15, in agreement with Best and Reid (1984). For $\delta_w = 1$, the value of λ_s increased significantly to 0.5, exceeding the other runs by a factor of 3–5, and causing an obvious shift in the shape of the separation zone.

3.3.5. Secondary Flow

Figure 15 illustrates the cross-sectional distribution of the velocity at various locations, such as near the floodplain step and downstream, highlighting the formation and progression of secondary flow. Table 6 illustrates the size and the temporal/spatial scales associated with a full rotation of helical cell. The observed downwelling flows in the floodplain step lee (Figure 15a, $x = -0.6$), which is a typical flow structure in backward-facing step flow, were consistent with past findings (Park et al., 2007). Moreover, as the width ratio

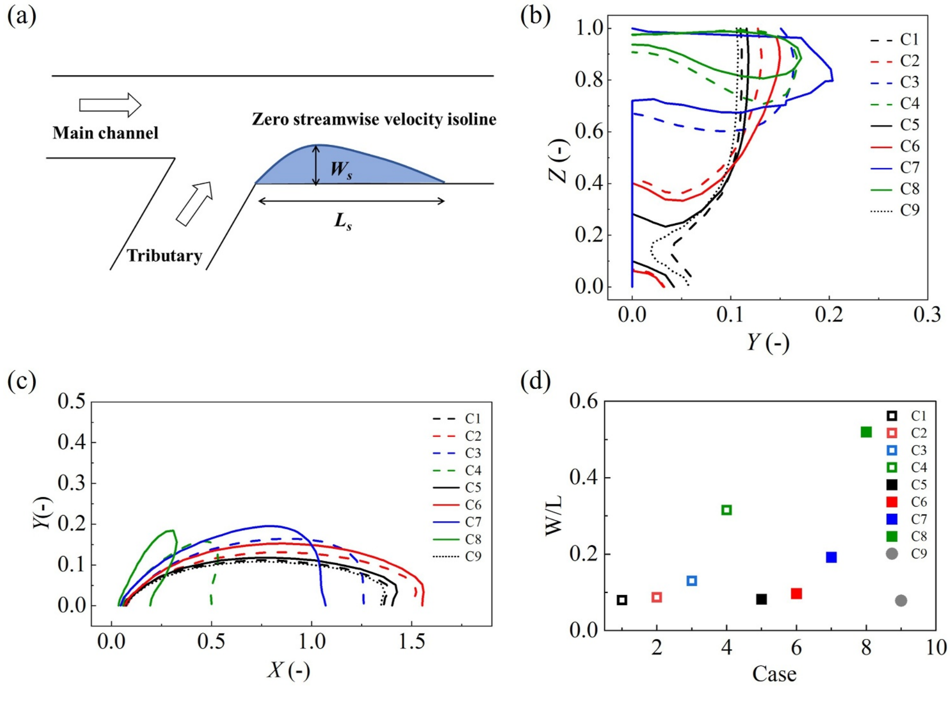

Figure 14. Characteristics of the separation zone: (a) conceptual model; (b) the shape of the maximum width of the separation zone in the y-z plane; (c) the shape of the maximum length of the separation zone in the x-y plane at $Z = 0.9$; (d) the shape index values of the separation zone λ_s.

Table 5
Size of the Separation Zone at Different Depths

Run	Depth Z (−)	Length L_s (m)	Width W_s (m)	L_s/W (−)	W_s/W (−)	W_s/L_s (−)	λ_s (−)
C1	0.9	0.582	0.047	1.386	0.112	0.081	0.080
	0.5	0.513	0.045	1.221	0.107	0.088	
	0.2	0.356	0.031	0.847	0.074	0.087	
C2	0.9	0.636	0.056	1.514	0.133	0.088	0.087
	0.5	0.465	0.043	1.107	0.102	0.092	
	0.2	0.217	0.024	0.517	0.057	0.111	
C3	0.9	0.526	0.071	1.252	0.169	0.135	0.130
	0.5	0.326	0.045	0.776	0.107	0.138	
	0.2	0.134	0.016	0.319	0.038	0.119	
C4	0.9	0.227	0.071	0.540	0.169	0.313	0.315
	0.5	0.048	0.012	0.114	0.029	0.250	
	0.2	0	0	0	0	0	
C5	0.9	0.591	0.05	1.407	0.119	0.085	0.082
	0.5	0.495	0.045	1.179	0.107	0.091	
	0.2	0.251	0.026	0.598	0.062	0.103	
C6 (F1)	0.9	0.652	0.065	1.552	0.155	0.100	0.097
	0.5	0.470	0.046	1.119	0.110	0.097	
	0.2	0.178	0.022	0.424	0.052	0.124	
C7	0.9	0.439	0.086	1.045	0.205	0.196	0.192
	0.5	0.243	0.031	0.579	0.074	0.128	
	0.2	0	0	0	0	0	
C8	0.9	0.135	0.076	0.321	0.181	0.563	0.520
	0.5	0	0	0	0	0	
	0.2	0	0	0	0	0	
C9 (F0)	0.9	0.571	0.043	1.351	0.102	0.075	0.079
	0.5	0.500	0.039	1.190	0.093	0.078	
	0.2	0.305	0.026	0.726	0.062	0.085	

δ_w increased, a complete secondary cell was evident, and its size ($0.2H$) corresponded to the height of the floodplain (Figures 15b–15d). Additionally, at the downstream junction corner ($X = 0.5$), the separation zone was presented by the black line in the inner bank, and a weak helical cell having a rotational velocity of 0.014–0.032 m/s (occupying 7%–16% U_m) was observed at $Y = 0.2$–0.4. As δ_w increased further, the secondary flow gradually shifted toward the inner bank and disrupted the separation zone near the bed (Figure 15c, $X = 0.5$). This showed a more pronounced upwelling near the inner bank, which increased the water surface level (Figure 10d).

The findings in Table 6 reveal that the intensity and scale of the secondary flow increased notably for $\delta_h = 0.5$. Specifically, for $\delta_h = 0.5$, $\delta_w = 1.0$, a considerably stronger secondary cell was observed, having a rotational velocity ranging from 0.042 to 0.105 m/s (occupying 21%–53% U_m) and occupying around 35% of the width of the post-confluence channel (Figure 15h). Moreover, the secondary flow core at $Z = 0.4$ was higher if compared to the runs for $\delta_h = 0.25$, suggesting that the location of the secondary flow may be related to the floodplain height. A similar phenomenon was observed as δ_w increased, with the secondary flow gradually moving toward the inner bank.

Additionally, it was observed that the location of the secondary cell varied toward downstream. A method based on the shape index of the main secondary flow within the cross-section was used (Li et al., 2022; Shen et al., 2022). It is noteworthy that the study has solely focused on the secondary flow dominant in the section, while weaker cells such as Cell one in the inner bank were neglected (Figure 9b). The core of the main secondary

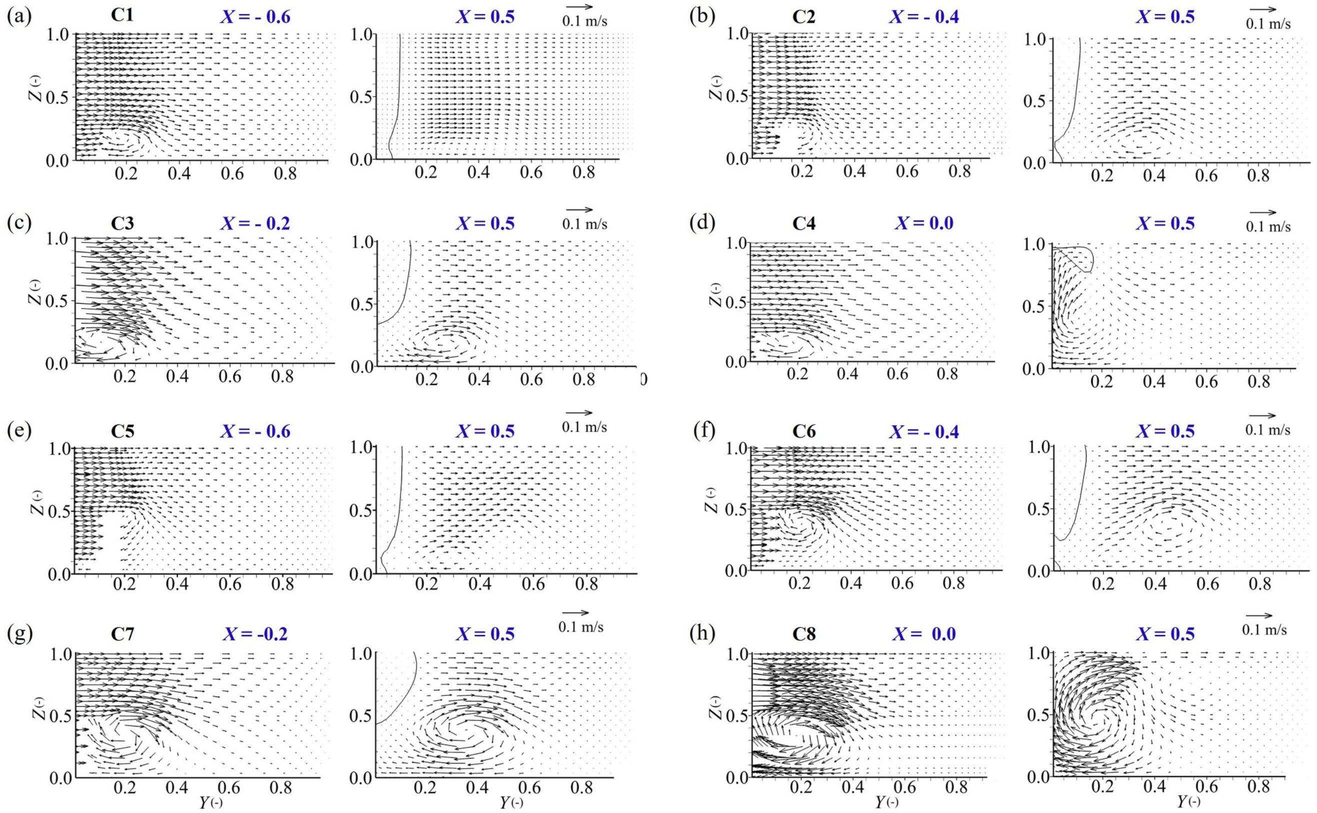

Figure 15. Secondary flow at the floodplain side (X = -0.6, 0.4, -0.2 and 0) and downstream of confluence (X = 0.5). Solid line delineates reverse flow zone.

flow was denoted by c in Figure 16a, with a and b representing the distances from c to the wall and bed, respectively.

Figure 16 shows the cross-sectional distribution of secondary flow at $X = -0.7$, -0.5, 0.0, 0.5, 1.0, 1.5, 2.0 and 3.0. The core of the secondary cell, denoted as c, was located near the floodplain step, that is, in the range of $0.20 < Y < 0.26$, for all Runs. As the flow developed downstream, the position of c gradually shifted toward different locations, being influenced by the floodplain size. In C1, c initially expanded to the center ($Y = 0.3$, $Z = 0.1$) before gradually moving toward the inner bank and upper flow ($Y = 0.2$, $Z = 0.3$) downstream. This can be attributed to the small streamline curvature associated with the tributary flow downstream. As the width ratio δ_w increased to 0.5, c was stable at $Y = 0.2$ and $Z = 0.18$, near the junction corner ($0 < X < 1$), before moving

Table 6
Size and Time/Length Scale for a Complete Rotation of Helical Cells

Run	Rotational velocity (−)	Width (−)	Height (−)	Timescale for complete rotation (s)	Length scale for complete rotation (m)
C1	0.09–0.17	0.14–0.19	0.05–0.10	6.04	1.21
C2	0.13–0.23	0.24–0.29	0.30–0.50	8.77	1.75
C3	0.16–0.37	0.24–0.33	0.50–0.60	6.96	1.39
C4	0.19–0.43	0.29–0.33	0.70–0.80	7.01	1.40
C5	0.14–0.22	0.14–0.19	0.05–0.15	4.52	0.90
C6	0.16–0.28	0.29–0.38	0.50–0.60	9.32	1.86
C7	0.19–0.41	0.33–0.43	0.50–0.75	7.71	1.54
C8	0.19–0.53	0.48–0.52	0.80–0.90	8.35	1.67
C9	0.19–0.16	0.14–0.19	0.05–0.10	6.83	1.31

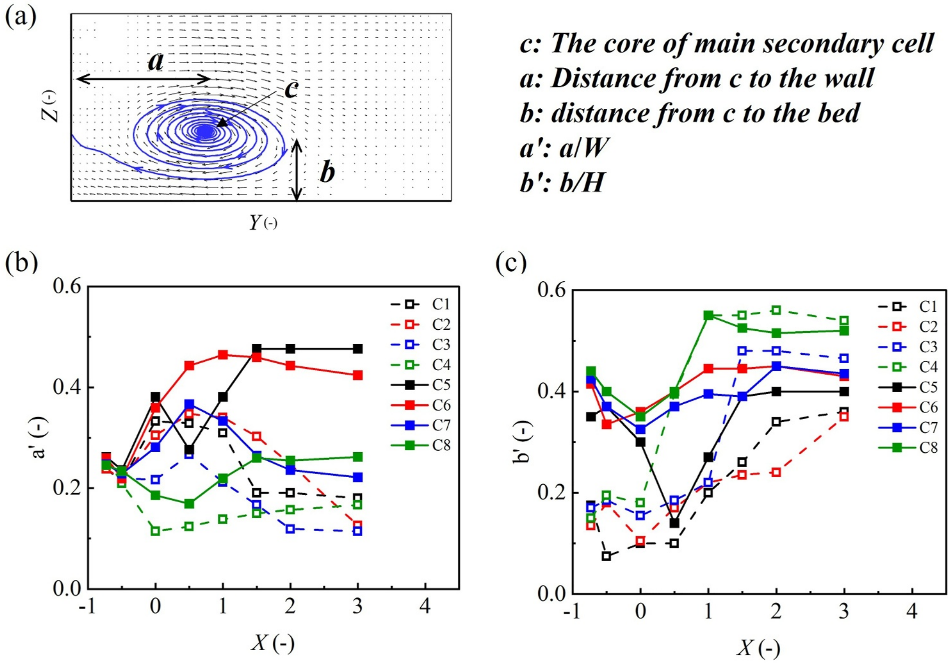

Figure 16. Formation and evolution of the secondary cell: (a) the definition of the secondary cell; (b) variation of distance of the main secondary cell core to the wall; (c) variation of distance of the secondary cell core to the bed.

toward the inner bank and upper flow ($Z = 0.5$). For $\delta_w = 1.0$, the secondary cell was observed to be closer to the inner bank. Furthermore, as δ_h increased to 0.5 (Figure 16c), the core c moved to $Z = 0.3$–0.4. In C5 and C6, it was located near at the center of the post-confluence channel ($Y = 0.45$). Additionally, the secondary cell moved toward the inner bank as the δ_w exceeded 0.5, which is consistent with a low height ratio ($\delta_h = 0.25$).

In summary, the secondary flow initially expanded toward the center of the channel and then turned back toward the inner bank, stabilizing in a high location ($Z \approx 0.4$) downstream. The width and height of the floodplain had a significant influence on this evolution, the secondary flow being closer to the inner bank with an increasing δ_w, while its height depended on the δ_h.

3.3.6. Turbulent Kinetic Energy

Figure 17 presents the distribution of TKE in different horizontal planes in the CHZ. The value of TKE is representative of the intensity of velocity fluctuations and its spatial extent indicates the size of the shear layers (Rhoads & Sukhodolov, 2008). The mixing layer with high TKE started in the vicinity of the upstream junction corner from the confluence of the main channel and tributary (identified as shear layer 1). TKE increased in shear layer 1 are associated with high turbulence production due to the high velocity difference between the main channel and tributary. Two kinds of shear layers were found below the floodplain in the C2 and C6: one is mixing layer 1, and the second one is the shear layer which forms between the confluence flow and the secondary cell in the lee of the floodplain step (identified as shear layer 2). Shear layer 1 was observed near the water surface and bed (Figure 17). Instead, the shear layer 2 was only found near the bed, which is likely due to the absence of a secondary cell at the water surface. An enhanced shear layer 2 was found at the boundary of the separation zone in C4, when the floodplain width ratio increased.

4. Discussion

4.1. Effect of Tributary Floodplain on Hydrodynamics

The present study contributes to a better understanding of the complex flow dynamics at an asymmetrical laboratory-scale confluence, with a focus on the influence of tributary floodplain topography. The simulations revealed that various flow features, such as secondary flows, separation zone, and shear layers, were significantly

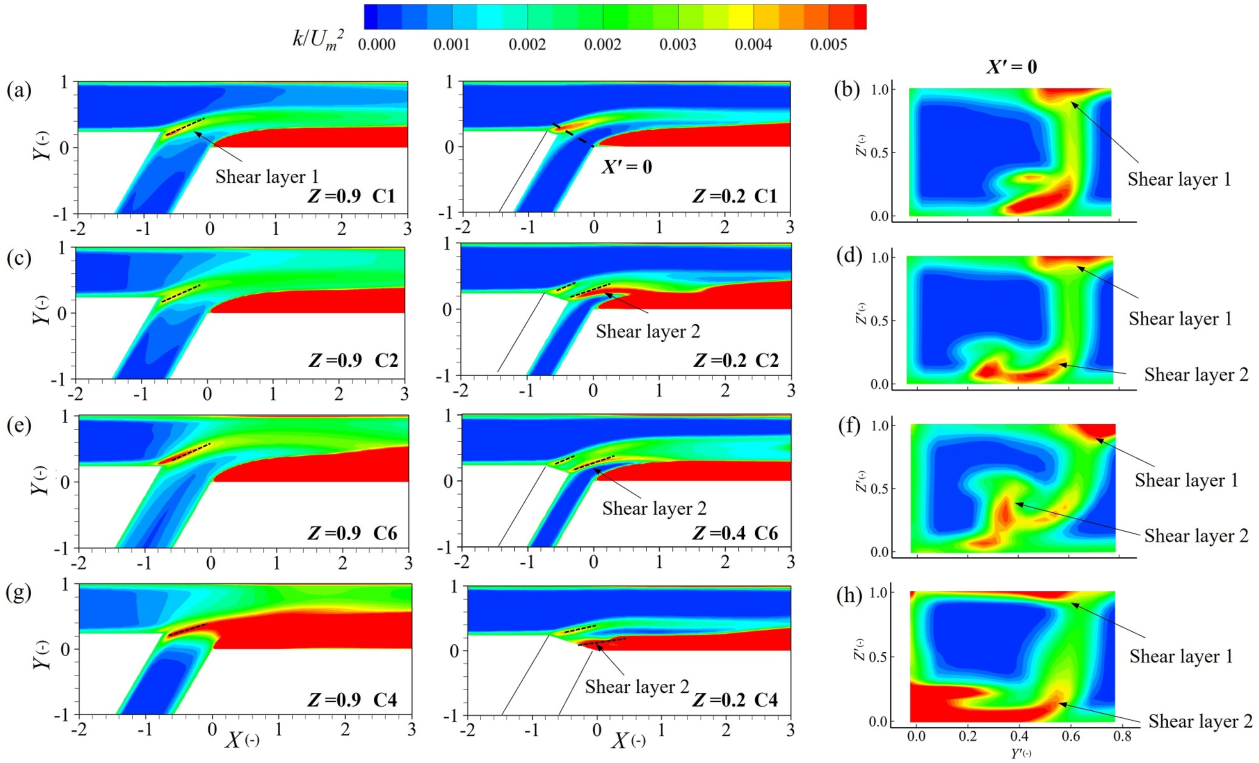

Figure 17. Distribution of the turbulent kinetic energy: (a, b) Run C1; (c, d) Run C2; (e, f) Run C6; (d, g) Run C4. The left column refers to the water surface ($Z = 0.9$) or near the floodplain ($Z = 0.2$ or 0.4), the right column is the cross-sectional velocity at $X' = 0$.

influenced by the size of the floodplain. Based on the numerical results obtained for different floodplain width ratios (δ_w) and height ratios (δ_h), the study proposes a conceptual model that can be applied to three different conditions: (a) confluence with narrow and low floodplain, (b) confluence with narrow and high floodplain, and (c) confluence with wide and high floodplain. The model offers useful insights into the impact of floodplain on flow dynamics in the CHZ (Figure 18).

In previous studies, the size of the separation zone in concordant confluences was found to be mainly related to three factors: the junction angle, the discharge ratio, and the Froude number (Gurram et al., 1997). Specifically, both the length and width of the separation zone increase as the junction angle and the discharge ratio increase, while the separation zone decreases with increasing Froude number. Through this study, it has been determined that the fixed topography of the river channel has a pivotal role in establishing the shape of the separation zone. The intricate and nonlinear relationship between the size of the floodplain and the dimensions of the separation zone is presented in Figure 14. It is noted that the length and width of the separation zone increased as δ_h and δ_w increased, primarily due to inflow from the tributary that possessed greater momentum, leading to pronounced flow separation downstream (Figures 18b and 18c). For $\delta_w = 0.5$, a 13% and 15% growth in the width and length of the separation zone occurred, respectively, in comparison to the case without floodplain (Figure 14). For the wider floodplain (Figure 18c), the separation zone was destroyed near the bed due to fluid upwelling, while the width of the separation zone increases by 77% and the length decreases by 76% near the water surface, resulting in a convex ellipse shape (Figure 18c). The width of the separation zone was higher due to the inflow from the tributary having greater momentum, and the decrease in the length of the separation zone is chiefly associated with the stronger upwelling generated by the floodplain step.

In a concordant confluence, the helical cells caused by the streamline curvature had about 8% of U_m at the post confluence channel (Yuan et al., 2023). However, two helical cells were clearly observed (Figure 18a), Cell 1 with 6% U_m in the inner bank was related to the streamline curvature as in a concordant bed confluence, Cell 2 with 15% U_m in the channel center mainly resulted from the cells in the lee of the floodplain step and streamline curvature, and the effects of the floodplain might play a more important role (Figure 9). For the narrow and high

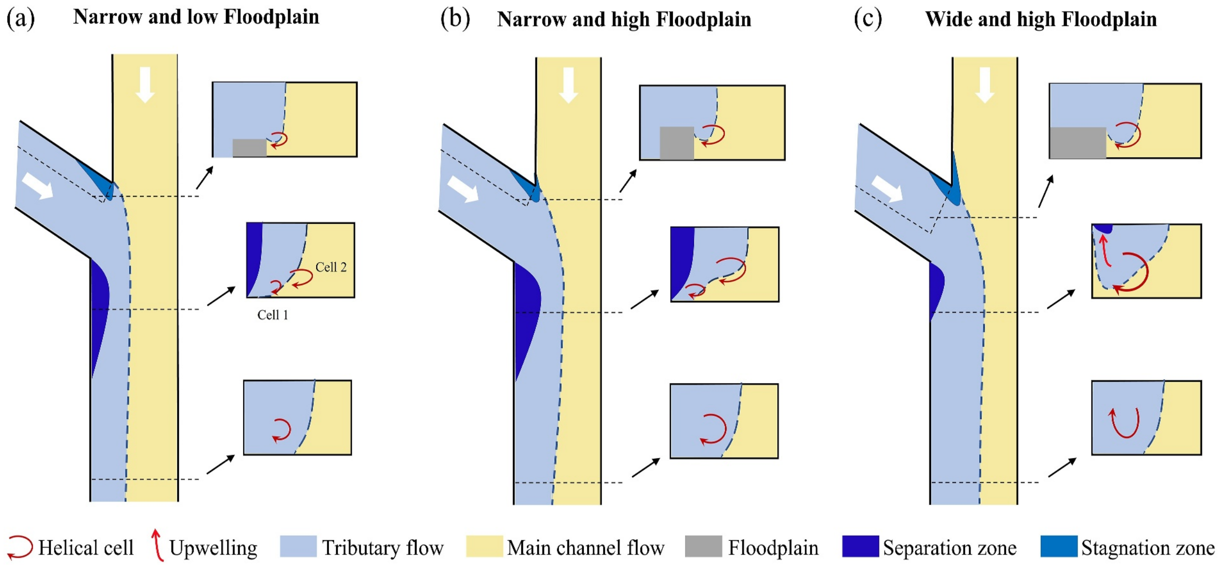

Figure 18. Conceptual model of hydrodynamics at confluence with tributary floodplain topography. (a) narrow and low Floodplain, (b) narrow and high Floodplain, and (c) wide and high Floodplain.

floodplain (Figure 18b), the size and intensity of the Cell 2 increased, primarily due to the flow separation exhibited by the tributary inflow at the brink of the floodplain step. The height of the Cell 2 also changed and was consistent with the height of the floodplain (Figure 16). However, the structure that two secondary cells coexisted was unstable, Cell 2 gradually moved to the inner bank and merged with Cell 1 downstream, leaving just one cell visible further downstream (Figures 18a and 18b). For the wide and high floodplain (Figure 18c), the stronger Cell 2 with 30% U_m and 35%W was located adjacent to the inner bank, which destroyed the Cell 1 and adjacent separation zone. A two-layer flow structure that the tributary flow mainly existed near the free surface and the main channel progressed near the bed was observed for the bed discordant ($\delta_w = 1.0$). However, a cross-sectional scale recirculation cell destroyed the two-layer flow structure (Canelas et al., 2022). In contrast to the findings of Canelas et al. (2022), the two-layer flow structure and the stronger secondary cell was found for C6 ($\delta_h = 0.5$ and $\delta_w = 1.0$). This is because the tributary and main channel flow had similar momentum, the two-layer flow structure was stable and not easily affected.

Two types of shear layers characterized by increased TKE levels were observed (Figure 17). The first, mostly vertical, shear layer (or mixing layer) originated at the junction of two flows, is a common feature in concordant confluences (Cheng & Constantinescu, 2020; Rhoads & Sukhodolov, 2008; Yuan et al., 2018). The second shear layer is formed between the tributary flow and the secondary circulation cell within the floodplain step, which is consistent with the observations of the foregoing experiments by Canelas et al. (2022) at discordant confluences. The mixing shear layer was comparatively weak and rapidly dissipated as the tributary inflow aligned with the deflected flow from the main channel. This can be explained that flow structures akin to Kelvin-Helmholtz instabilities within the mixing layer rapidly lose their coherence once they move away from the stagnation zone (Guillén-Ludeña et al., 2017). The location of the second shear layer mainly depended on the width of the tributary floodplain at the downstream edge of the floodplain step, and they moved to the inner bank downstream accompanied by the secondary flow.

4.2. Comparative Analysis

Past field studies have revealed that when the tributary acts as a compound channel the flow structure at the confluence is modified (Marinho et al., 2022; Yuan et al., 2021). Several features of the secondary cell, stagnation zone and separation zone were analyzed for the confluence between the Yangtze River and the Poyang Lake for both emerged/submerged floodplain (Li et al., 2022). During low flow conditions, as the tributary channel acts as a single channel with the emerged floodplain, the planform streamline curvature leads to a channel-scale secondary flow; during high flow conditions, as the tributary channel acts as a compound channel, a dual counter-rotating helical cell similar in magnitude was observed associated with the combined effects of the planform

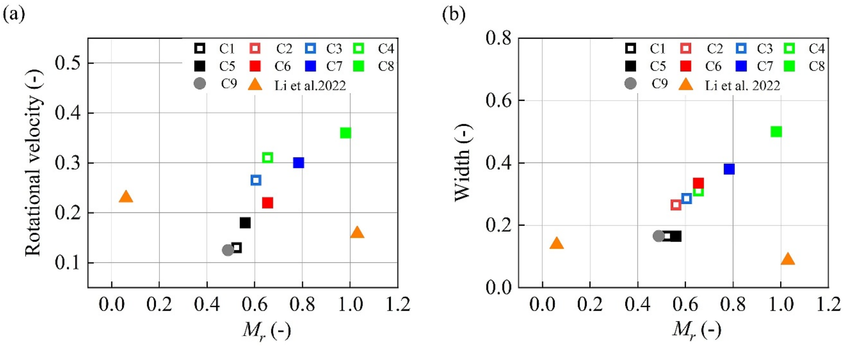

Figure 19. Rotational velocity (a) and width (b) of the secondary cell versus the momentum flux ratio. The rotational velocity and the width were non-dimensionalized using the average velocity and the post-confluence channel width, respectively.

curvature and penetration of Yangtze River flow into the Poyang Lake side (Li et al., 2022). Similar results also were observed in the present study. However, the intensity and magnitude of the double secondary cell in the flume were very different (Figure 9). The secondary cell formed by the streamline curvature was weak and disappeared downstream due to the flow redistribution and the interference with another cell. Figure 19 shows that at the laboratory confluence scale the rotational velocity and the width of the secondary cell increased with the increase of the momentum ratio (M_r). In the field confluence, the rotational velocity and the width of the secondary cell was inversely associated with the momentum ratio. At the lower M_r, the large curvature of streamlines allowed a strong penetration from the high-velocity Yangtze River flow, resulting in a more powerful secondary cell (22%U_m).

At the confluence between the Yangtze River and the Poyang Lake, the size of the stagnation zone increased as the momentum ratio ($M_r < 1$) increased, which is basically consistent with the present study (Figure 14). However, the stagnation zone gradually decreased when $M_r > 1$, which implies that the significant flow velocity difference does not favor the formation of the stagnation zone. In addition, at the Yangtze River-Poyang Lake confluence, the separation zone was not clearly identified also as the junction angle is not sharp like the laboratory flume, and the secondary flow had little effect on the separation zone due to the larger width of the Yangtze River. The complex hydrodynamics associated with the floodplain in the Poyang Lake also affect the sediment transport, morphological features, mixing patterns and fish habitat (Xu et al., 2022; Yuan et al., 2021, 2023). In summary, although the flume experiments and field observations shared some characteristics, some key differences were also observed, and a more detailed investigation of the floodplain is still needed to identify scale effects.

The flume experiments and numerical simulations were conducted in a simple yet representative confluence, to provide a first step toward understanding how the tributary floodplain can affect the hydrodynamics of a confluence. Nonetheless, in large-scale river confluences tributaries might have more complex topological structures than that of the present study.

5. Conclusions

The present study combines laboratory experiments and numerical simulations of a laboratory-scale confluence to investigate the hydrodynamic response of a channel flow confluence to the tributary floodplain topography, focusing on the effects of the width and height of the floodplain. The mechanism of the formation of the separation zone, secondary circulation and shear layers was analyzed in detail. Additionally, the results were synthesized into a conceptual model to summarize the commonalities and differences in the hydrodynamics of confluence with a different tributary floodplain topography. The main conclusions are as follows:

1. With the floodplain existing, two kinds of secondary circulations were identified at confluence zone: one was due to the tributary streamline curvature, and the other is produced by flow separation at the brink of the floodplain step lee.
2. An increase in the floodplain size enhanced the strength of the secondary cell in the compound tributary channel, but it disappeared near the junction because of the effects of the main channel.

3. The size of the separation zone (reverse flow zone) and the intensity of the secondary circulations increased as the floodplain size increased, due to the decreased tributary cross-sectional area which increases flow momentum, resulting in a larger tributary flow deflection and centrifugal force downstream.
4. For the wide floodplain (close to discordant bed), strong secondary circulations occupied the cross-sectional area which can destroy lower water surface separation zone caused by energy loss and negative pressure, resulting in local rise of the water surface.
5. These secondary circulations first formed in the floodplain step lee and longitudinally evolved before eventually stabilizing. The location was closer to the inner bank as the floodplain width increased, while their height depended on the floodplain height.
6. Two kinds of shear layers were found if the effects of the tributary floodplain were strong: a mixing layer was observed near the water surface and bed, and second shear layer placed near the bed formed the confluence flow and the secondary circulation in the floodplain step lee.
7. A conceptual model of confluence with tributary floodplain based on the prominent hydrodynamic characteristic was proposed to summarize the commonalities and the differences in hydrodynamics features between the present laboratory-scale confluence and the large-scale confluence between the Yangtze River and the Poyang Lake.

Appendix A: RSM Model

The exact transport equations for the transport of the Reynolds stresses can be written as follows:

$$\frac{\partial}{\partial t}\left(\overline{u_i' u_j'}\right) + \frac{\partial}{\partial x_k}\left(u_k \overline{u_i' u_j'}\right) = D_{Tij} + D_{Lij} + P_{ij} + \Pi_{ij} + E_{ij} + F_{ij} \tag{A1}$$

where D_{Tij} is turbulent diffusion term, D_{Lij} is molecular diffusion term, P_{ij} is Reynolds stress production term, Π_{ij} is the (quadratic) pressure-strain term, E_{ij} is the dissipation term and F_{ij} is the production term by system rotation.

$$D_{Tij} = -\frac{1}{\rho}\frac{\partial}{\partial x_k}\overline{P'\left(\delta_{kj}u_i' + \delta_{ik}u_j'\right)} - \frac{\partial \overline{u_i' u_j' u_k'}}{\partial x_k} = \frac{\partial}{\partial x_k}\left(\frac{\nu_t}{\sigma_k}\frac{\partial \overline{u_i' u_j'}}{\partial x_k}\right) \tag{A2}$$

$$D_{Lij} = \nu \frac{\partial}{\partial x_k}\left(\frac{\partial}{\partial x_k}\overline{u_i' u_j'}\right) \tag{A3}$$

$$P_{ij} = -\left(\overline{u_i' u_k'}\frac{\partial u_j}{\partial x_k} + \overline{u_j' u_k'}\frac{\partial u_i}{\partial x_k}\right) \tag{A4}$$

$$\Pi_{ij} = \frac{P'}{\rho}\left(\frac{\partial u_i'}{\partial x_j} + \frac{\partial u_j'}{\partial x_i}\right) = -C_1\frac{\varepsilon}{k}\left(\overline{u_i' u_j'} - \frac{2}{3}k\delta_{ij}\right) - C_2\left(P_{ij} - \frac{2}{3}P\delta_{ij}\right) \tag{A5}$$

$$E_{ij} = -2\mu\overline{\frac{\partial u_i'}{\partial x_k}\frac{\partial u_j'}{\partial x_k}} \tag{A6}$$

$$F_{ij} = -2\Omega_k\left(\overline{u_j' u_m'}\varepsilon_{ikm} + \overline{u_i' u_m'}\varepsilon_{jkm}\right) \tag{A7}$$

where σ_k, C_1,C_2 are empirical constants with the values of 0.09,1.8, and 0.6; $\delta_{ij} = 1$ when $i = j$ and 0 when $i \neq j$; Ω_k is the rotation vector; $\varepsilon_{ijk} = 1$ if i, j, and k are in cyclic order and different, $\varepsilon_{ijk} = -1$ if i, j, and k are in anti-cyclic order and different, and $\varepsilon_{ijk} = 0$ in case that any two indices are the same.

The dissipation rate ε, is calculated from the following transport equation:

$$\frac{\partial \varepsilon}{\partial t} + \frac{\partial \varepsilon u_i}{\partial x_i} = \frac{\partial}{\partial x_i}\left[\left(\frac{\nu_t}{\sigma_k} + \nu\right)\frac{\partial \varepsilon}{\partial x_i}\right] + C_{1\varepsilon}\frac{\varepsilon}{k}G_k - C_{2\varepsilon}\frac{\varepsilon^2}{k} \tag{A8}$$

10.1029/2023WR036244

$$G_k = -\rho \overline{u_i' u_j'} \frac{\partial u_j}{\partial x_i} = \nu_t \left(\frac{\partial u_i}{\partial x_j} + \frac{\partial u_j}{\partial x_i} \right) \tag{A9}$$

$$\nu_t = C_u \frac{k^2}{\varepsilon} \tag{A10}$$

where $C_{\varepsilon 1}$, $C_{\varepsilon 2}$ and C_u are empirical coefficients with values of 1.44, 1.92 and 0.0845.

Appendix B: Mesh Sensitivity Analysis

Mesh 1 (Coarse Mesh): the size of a single cell upstream of the junction and in the post-confluence channel $\Delta x \times \Delta y \times \Delta z$ was 50*20*20 mm and 25*20*20 mm close to the walls, and the total number of cells was 124,775. Mesh 2 (Medium Mesh): upstream of the junction and in the post-confluence channel the size of a single cell in the $\Delta x \times \Delta y \times \Delta z$ was 30*11*8 mm and 15*11*8 mm close to the walls, and the total number of cells was 731,844. Mesh 3 (Fine Mesh): upstream of the junction and in the post-confluence channel the size of a single cell $\Delta x \times \Delta y \times \Delta z$ was 25*11*8 mm and 10*11*8 mm close to the walls, and the total number of cells was 1,178,152.

Figure B1 shows a comparison between experimental data and numerical results for those three meshes. For the streamwise velocity *u*, the numerical results for the three different meshes were not significantly different and relatively close to the experimental data. For the lateral velocity *v* and vertical velocity *w*, the numerical results for Mesh 1 were poor and could not capture the maximum velocity. The results of Mesh 2 and Mesh 3 were similar, and both had a good agreement with the experimental data.

Figure B2 compares the secondary flow between experimental data and numerical results for those three meshes. Mesh 1 deviated too much from the experimental data in that there was simply a noticeable lateral flow, but a not complete secondary flow formed. Mesh 2 and Mesh 3 had secondary flows whose position and magnitude align with the experimental results. Considering the computational speed, the Mesh 2 was selected for the numerical model used in this study.

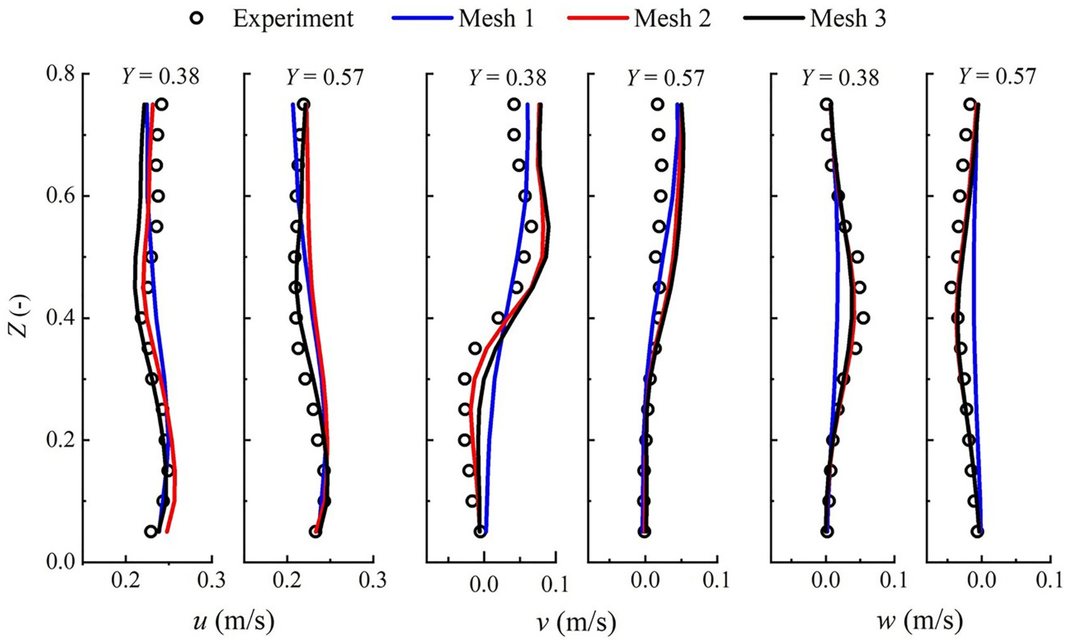

Figure B1. The mesh sensitivity analysis results for Run F1: (a) streamwise velocity, (b) lateral velocity and (c) vertical velocity ($X = 0.3$).

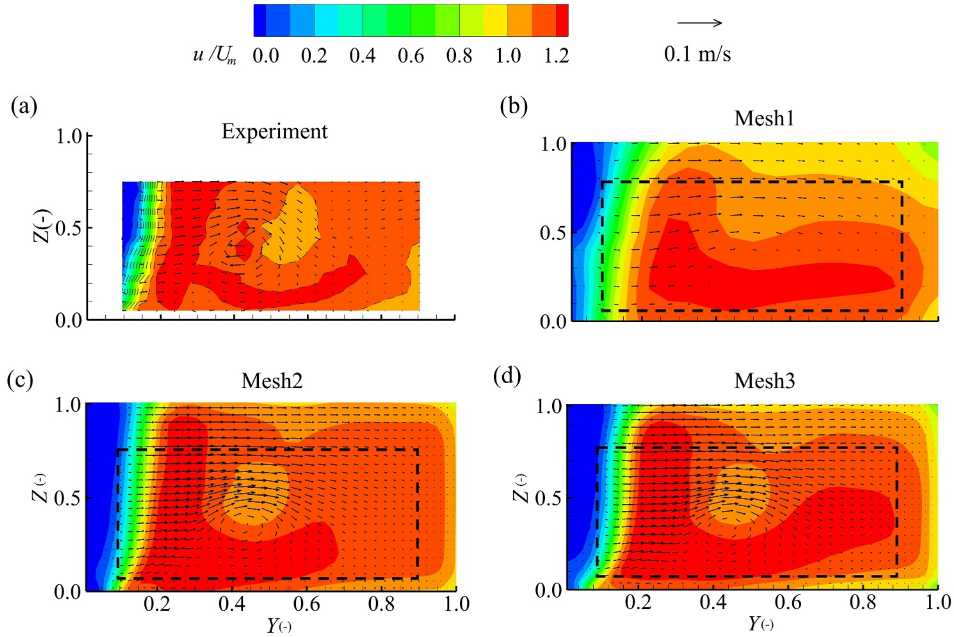

Figure B2. Mesh sensitivity analysis of the secondary flow cells and the longitudinal velocity distribution: (a) experimental data, (b) Mesh1, (c) Mesh2 and (d) Mesh3 ($X = 0.3$).

Data Availability Statement

The data are available for download: https://doi.org/10.5281/zenodo.8373874. The software version used in this paper is ANSYS, 2021 R2, which is available for download at the link: https://www.ansys.com/products/fluids/ansys-fluent.

Acknowledgments
This research was funded by the Fundamental Research Funds for the Central Universities (B230201057).

References

ANSYS. (2021). *ANSYS fluent 2021 R2*. ANSYS Inc.

Best, J. L. (1987). Flow dynamics at river channel confluences: Implications for sediment transport and bed morphology. In F. G. Ethridge, et al (Eds.), *Recent developments in fluvial sedimentology* (Vol. 39, pp. 27–35). The Society of Economic Paleontologists and Mineralogists. https://doi.org/10.2110/pec.87.39.0027

Best, J. L., & Reid, I. (1984). Separation zone at open-channel junctions. *Journal of Hydraulic Engineering*, *110*(11), 1588–1594. https://doi.org/10.1061/(ASCE)0733-9429(1984)110:11(1588)

Best, J. L., & Roy, A. G. (1991). Mixing-layer distortion at the confluence of channels of different depth. *Nature*, *350*(6317), 411–413. https://doi.org/10.1038/350411a0

Biron, P. M., Best, J. L., & Roy, A. G. (1996). Effects of bed discordance on flow dynamics at open channel confluences. *Journal of Hydraulic Engineering*, *122*(12), 676–682. https://doi.org/10.1061/(ASCE)0733-9429(1996)122:12(676)

Blocken, B., & Gualtieri, C. (2012). Ten iterative steps for model development and evaluation applied to computational fluid dynamics for environmental fluid mechanics. *Environmental Modelling & Software*, *33*, 1–22. https://doi.org/10.1016/j.envsoft.2012.02.001

Bradbrook, K. F., Richards, K. S., Biron, P. M., & Roy, A. G. (2001). Role of bed discordance at asymmetrical river confluences. *Journal of Hydraulic Engineering*, *127*(5), 351–368. https://doi.org/10.1061/(ASCE)0733-9429(2001)127:5(351)

Canelas, O. B., Ferreira, R. M. L., & Cardoso, A. H. (2022). Hydro-morphodynamics of an open-channel confluence with bed discordance at dynamic equilibrium. *Water Resources Research*, *58*(1). https://doi.org/10.1029/2021wr029631

Canelas, O. B., Ferreira, R. M. L., Guillén-Ludeña, S., Alegria, F. C., & Cardoso, A. H. (2020). Three-dimensional flow structure at fixed 70° open-channel confluence with bed discordance. *Journal of Hydraulic Research*, *58*(3), 434–446. https://doi.org/10.1080/00221686.2019.1596988

Cheng, Z., & Constantinescu, G. (2020). Stratification effects on hydrodynamics and mixing at a river confluence with discordant bed. *Environmental Fluid Mechanics*, *20*(4), 843–872. https://doi.org/10.1007/s10652-019-09725-6

Constantinescu, G., Miyawaki, S., Rhoads, B., & Sukhodolov, A. (2012). Numerical analysis of the effect of momentum ratio on the dynamics and sediment-entrainment capacity of coherent flow structures at a stream confluence. *Journal of Geophysical Research*, *117*(F4). https://doi.org/10.1029/2012JF002452

De Morais, E. S., Dos Santos, M. L., Cremon, E. H., & Stevaux, J. C. (2016). Floodplain evolution in a confluence zone: Paraná and ivaí rivers, Brazil. *Geomorphology*, *257*, 1–9. https://doi.org/10.1016/j.geomorph.2015.12.017

Duguay, J., Biron, P. M., & Lacey, J. (2022). Aerial observations and numerical simulations confirm density-driven streamwise vortices at a river confluence. *Water Resources Research*, *58*(7). https://doi.org/10.1029/2021WR031527

Fatchurrohman, N., & Chia, S. T. (2017). Performance of hybrid Nano-micro reinforced mg metal matrix composites brake caliper: Simulation approach. *IOP Conference Series: Materials Science and Engineering*, *257*, 012060–012061. https://doi.org/10.1088/1757-899X/257/1/012060

Ford, W. I., Fox, J. F., Mahoney, D. T., Degraves, G., Erhardt, A., & Yost, S. (2020). Backwater confluences of the Ohio River: Organic and inorganic fingerprints explain sediment dynamics in wetlands and marinas. *Journal of the American Water Resources Association*, *56*(4), 692–711. https://doi.org/10.1111/1752-1688.12850

Gaudet, J. M., & Roy, A. G. (1995). Effect of bed morphology on flow mixing length at river confluences. *Nature*, *373*(6510), 138–139. https://doi.org/10.1038/373138a0

Gibson, M. M., & Launder, B. E. (1978). Ground effects on pressure fluctuations in the atmospheric boundary layer. *Journal of Fluid Mechanics*, *86*(3), 491–511. https://doi.org/10.1017/S0022112078001251

Gualtieri, C., Abdi, R., Ianniruberto, M., Filizola, N., & Endreny, T. A. (2020). A 3D analysis of spatial habitat metrics about the confluence of Negro and Solimões rivers, Brazil. *Ecohydrology*, *13*(1), e2166. https://doi.org/10.1002/eco.2166

Gualtieri, C., Ianniruberto, M., & Filizola, N. (2019). On the mixing of rivers with a difference in density: The case of the Negro/Solimões confluence, Brazil. *Journal of Hydrology*, *578*, 124029. https://doi.org/10.1016/j.jhydrol.2019.124029

Guillen-Ludena, S., Cheng, Z., Constantinescu, G., & Franca, M. J. (2017). Hydrodynamics of mountain-river confluences and its relationship to sediment transport. *Journal of Geophysical Research-Earth Surface*, *122*(4), 901–924. https://doi.org/10.1002/2016jf004122

Guillen-Ludena, S., Franca, M. J., Cardoso, A. H., & Schleiss, A. J. (2015). Hydro-morphodynamic evolution in a 90 degrees movable bed discordant confluence with low discharge ratio. *Earth Surface Processes and Landforms*, *40*(14), 1927–1938. https://doi.org/10.1002/esp.3770

Gurram, S. K., Karki, K. S., & Hager, W. H. (1997). Subcritical junction flow. *Journal of Hydraulic Engineering*, *123*(5), 447–455. https://doi.org/10.1061/(ASCE)0733-9429(1997)123:5(447)

Hamidifar, H., Omid, M. H., & Keshavarzi, A. (2016). Kinetic energy and momentum correction coefficients in straight compound channels with vegetated floodplain. *Journal of Hydrology*, *537*, 10–17. https://doi.org/10.1016/j.jhydrol.2016.03.024

Hirt, C. W., & Nichols, B. D. (1981). Volume of fluid (VOF) method for the dynamics of free boundaries. *Journal of Computational Physics*, *39*(1), 201–225. https://doi.org/10.1016/0021-9991(81)90145-5

Issa, R. I. (1986). Solution of the implicitly discretized fluid flow equations by operator-splitting. *Journal of Computational Physics*, *62*(1), 40–65. https://doi.org/10.1016/0021-9991(86)90099-9

Jin, T., Ramos, P. X., Mignot, E., Riviere, N., & De Mulder, T. (2023). On the delineation of the flow separation zone in open-channel confluences. *Advances in Water Resources*, *180*, 104525. https://doi.org/10.1016/j.advwatres.2023.104525

Leite Ribeiro, M. B. K., Roy, A. G., & Schleiss, A. J. (2012). Flow and sediment dynamics in channel confluences. *Journal of Geophysical Research*, *117*(F1). https://doi.org/10.1029/2011jf002171

Li, K., Tang, H., Yuan, S., Xiao, Y., Xu, L., Huang, S., et al. (2022). A field study of near-junction-apex flow at a large river confluence and its response to the effects of floodplain flow. *Journal of Hydrology*, *610*, 127983. https://doi.org/10.1016/j.jhydrol.2022.127983

Luo, H., Fytanidis, D. K., Schmidt, A. R., & García, M. H. (2018). Comparative 1D and 3D numerical investigation of open-channel junction flows and energy losses. *Advances in Water Resources*, *117*, 120–139. https://doi.org/10.1016/j.advwatres.2018.05.012

Maranzoni, A., & Tomirotti, M. (2021). 3D CFD analysis of the performance of oblique and composite side weirs in converging channels. *Journal of Hydraulic Research*, *59*(4), 586–604. https://doi.org/10.1080/00221686.2020.1818304

Marinho, R. R., Furtado, A. R., Dos Santos, V. C., Nascimento, A. Z. A., & Filizola Junior, N. (2022). Riverbed morphology and hydrodynamics in the confluence of complex mega rivers-A study in the Branco and Negro rivers, Amazon basin. *Journal of South American Earth Sciences*, *118*, 103969. https://doi.org/10.1016/j.jsames.2022.103969

Messager, M. L., Lehner, B., Cockburn, C., Lamouroux, N., Pella, H., Snelder, T., et al. (2021). Global prevalence of non-perennial rivers and streams. *Nature*, *594*(7863), 391–397. https://doi.org/10.1038/s41586-021-03565-5

Momplot, A., Lipeme Kouyi, G., Mignot, E., Rivière, N., & Bertrand-Krajewski, J. L. (2017). Typology of the flow structures in dividing open channel flows. *Journal of Hydraulic Research*, *55*(1), 63–71. https://doi.org/10.1080/00221686.2016.1212409

Mosley, M. P. (1976). An experimental study of channel confluences. *The Journal of Geology*, *84*(5), 535–562. https://doi.org/10.1086/628230

Mu, S., Yang, G., Xu, X., Wan, R., & Li, B. (2022). Assessing the inundation dynamics and its impacts on habitat suitability in Poyang Lake based on integrating Landsat and MODIS observations. *Science of the Total Environment*, *834*, 154936. https://doi.org/10.1016/j.scitotenv.2022.154936

Ouro, P., Fraga, B., Viti, N., Angeloudis, A., Stoesser, T., & Gualtieri, C. (2018). Instantaneous transport of a passive scalar in a turbulent separated flow. *Environmental Fluid Mechanics*, *18*(2), 487–513. https://doi.org/10.1007/s10652-017-9567-3

Palmer, M., & Ruhi, A. (2019). Linkages between flow regime, biota, and ecosystem processes: Implications for river restoration. *Science*, *365*(6459), eaaw2087. https://doi.org/10.1126/science.aaw208

Park, H., Jeon, W. P., Choi, H., & Yoo, J. Y. (2007). Mixing enhancement behind a backward-facing step using tabs. *Physics of Fluids*, *19*(10), 105103. https://doi.org/10.1063/1.2781597

Proust, S., & Nikora, V. (2020). Compound open-channel flows: Effects of transverse currents on the flow structure. *Journal of Fluid Mechanics*, *885*, A24. https://doi.org/10.1017/jfm.2019.973

Rhoads, B. L., Riley, J. D., & Mayer, D. R. (2009). Response of bed morphology and bed material texture to hydrological conditions at an asymmetrical stream confluence. *Geomorphology*, *109*(3–4), 161–173. https://doi.org/10.1016/j.geomorph.2009.02.029

Rhoads, B. L., & Sukhodolov, A. N. (2004). Spatial and temporal structure of shear-layer turbulence at a stream confluence. *Water Resources Research*, *6*, 2393–2410. https://doi.org/10.1029/2003WR002811

Rhoads, B. L., & Sukhodolov, A. N. (2008). Lateral momentum flux and the spatial evolution of flow within a confluence mixing interface. *Water Resources Research*, *44*(8). https://doi.org/10.1029/2007WR006634

Schindfessel, L., Creëlle, S., & De Mulder, T. (2017). How different cross-sectional shapes influence the separation zone of an open-channel confluence. *Journal of Hydraulic Engineering*, *143*(9), 04017036. https://doi.org/10.1061/(ASCE)HY.1943-7900.0001336

Shen, X., Li, R., Cai, H., Feng, J., & Wan, H. (2022). Characteristics of secondary flow and separation zone with different junction angle and flow ratio at river confluences. *Journal of Hydrology*, *614*, 128537. https://doi.org/10.1016/j.jhydrol.2022.128537

Singh, P., Tang, X., & Rahimi, H. R. (2020). A computational study of interaction of main channel and floodplain: Open channel flows. *Journal of Applied Mathematics and Physics*, *8*(11), 2526–2539. https://doi.org/10.4236/jamp.2020.811188

Sukhodolov, A. N., Shumilova, O. O., Constantinescu, G. S., Lewis, Q. W., & Rhoads, B. L. (2022). Mixing dynamics at river confluences governed by intermodal behaviour. *Nature Geoscience*, *16*, 1–5. https://doi.org/10.1038/s41561-022-01091-1

Sukhodolov, A. N., & Sukhodolova, T. A. (2019). Dynamics of flow at concordant gravel bed river confluences: Effects of junction angle and momentum flux ratio. *Journal of Geophysical Research: Earth Surface*, *124*(2), 588–615. https://doi.org/10.1029/2018JF004648

Tang, H., Yuan, S., & Cao, H. (2022). Theory and practice of hydrodynamic reconstruction in plain river networks. *Engineering*, *24*, 202–211. https://doi.org/10.1016/j.eng.2022.01.015

Tang, H., Zhang, H., & Yuan, S. (2018). Hydrodynamics and contaminant transport on a degraded bed at a 90-degree channel confluence. *Environmental Fluid Mechanics*, *18*(2), 443–463. https://doi.org/10.1007/s10652-017-9562-8

Tonkin, J. D., Altermatt, F., Finn, D. S., Heino, J., Olden, J. D., Pauls, S. U., & Lytle, D. A. (2018). The role of dispersal in river network metacommunities: Patterns, processes, and pathways. *Freshwater Biology*, *63*(1), 141–163. https://doi.org/10.1111/fwb.13037

Vári, Á., Podschun, S. A., Erős, T., Hein, T., Pataki, B., Iojă, I. C., et al. (2022). Freshwater systems and ecosystem services: Challenges and chances for cross-fertilization of disciplines. *Ambio*, *51*(1), 135–151. https://doi.org/10.1007/s13280-021-01556-4

Wormleaton, P. R. (1996). Floodplain secondary circulation as a mechanism for flow and shear stress redistribution in straight compound channels. In *Coherent flow structures in open channels* (pp. 581–608). Wiley.

Xu, L., Yuan, S., Tang, H., Qiu, J., Xiao, Y., Whittaker, C., & Gualtieri, C. (2022). Mixing dynamics at the large confluence between the Yangtze River and Poyang Lake. *Water Resources Research*, *58*(11), e2022WR032195. https://doi.org/10.1029/2022WR032195

Yang, Q., Wang, X., Lu, W., & Wang, X. (2009). Experimental study on characteristics of separation zone in confluence zones in rivers. *Journal of Hydrologic Engineering*, *14*(2), 166–171. https://doi.org/10.1061/(ASCE)1084-0699(2009)14:2(166)

Yuan, S., Tang, H., Li, K., Xu, L., Gualtieri, C., Rennie, C., & Melville, B. (2021). Hydrodynamics, sediment transport and morphological features at the confluence between the Yangtze River and the Poyang Lake. *Water Resources Research*, *57*(3). https://doi.org/10.1029/2020WR028284

Yuan, S., Tang, H., Xiao, Y., Qiu, X., & Xia, Y. (2018). Water flow and sediment transport at open-channel confluences: An experimental study. *Journal of Hydraulic Research*, *56*(3), 333–350. https://doi.org/10.1080/00221686.2017.1354932

Yuan, S., Xu, L., Tang, H., Xiao, Y., & Gualtieri, C. (2022). The dynamics of river confluences and their effects on the ecology of aquatic environment: A review. *Journal of Hydrodynamics*, *34*, 1–14. https://doi.org/10.1007/s42241-022-0001-z

Yuan, S., Xu, L., Tang, H., Xiao, Y., & Whittaker, C. (2022). Swimming behavior of juvenile silver carp near the separation zone of a channel confluence. *International Journal of Sediment Research*, *37*(1), 122–127. https://doi.org/10.1016/j.ijsrc.2021.08.002

Yuan, S., Yan, G., Tang, H., Xiao, Y., Rahimi, H., Aye, M. N., & Gualtieri, C. (2023). Effects of tributary floodplain on confluence hydrodynamics. *Journal of Hydraulic Research*, *61*(4), 552–572. https://doi.org/10.1080/00221686.2023.2231413

Yuan, S., Zheng, Y., Tang, H., Chen, Y., Xu, L., Whittaker, C., & Gualtieri, C. (2024). Large wood transport and accumulation near the separation zone of a channel confluence. *Water Resources Research*, *60*(3), e2023WR034790. https://doi.org/10.1029/2023WR034790

Zhang, Z., Chen, X., Xu, C. Y., Hong, Y., Hardy, J., & Sun, Z. (2015). Examining the influence of river–lake interaction on the drought and water resources in the Poyang Lake basin. *Journal of Hydrology*, *522*, 510–521. https://doi.org/10.1016/j.jhydrol.2015.01.008